

# **Recent Progress in High Performance Cathodes for Aqueous Zinc Ion Batteries**

## **Abstract**

Aqueous zinc ion batteries (AZIBs) have been garnering interest as the successor to current battery technologies. Zinc is a cheap and abundant metal with aqueous electrolytes offering safe, non-flammable and eco-friendly systems, with large power outputs, storage capacities and long lifetimes. While there is a large diversity of cathodes for AZIBs, this review summarises recent research in manganese, vanadium, Prussian blue analogues and other transition metal and organic materials for use as cathodes in AZIBs. Insights into charge storage mechanisms and relevant electrochemical data is provided. Finally, opinions on future avenues of research are offered.

# Contents

<b>1</b>	<b>Introduction .....</b>	<b>5</b>
<b>2</b>	<b>MnO<sub>2</sub>-based.....</b>	<b>7</b>
2.1	$\alpha$ -MnO <sub>2</sub> .....	8
2.2	$\beta$ -MnO <sub>2</sub> .....	9
2.3	$\delta$ -MnO <sub>2</sub> .....	10
2.4	$\gamma$ -MnO <sub>2</sub> .....	11
2.5	Mn <sub>3</sub> O <sub>4</sub> .....	13
2.6	Other Mn-based Cathodes .....	15
<b>3</b>	<b>Vanadium-based .....</b>	<b>16</b>
3.1	Vanadium Oxides .....	16
3.1.1	V <sub>2</sub> O <sub>5</sub> .....	17
3.1.2	VO <sub>2</sub> (B).....	18
3.1.3	V <sub>3</sub> O <sub>7</sub> ·H <sub>2</sub> O (H <sub>2</sub> V <sub>3</sub> O <sub>8</sub> ).....	20
3.1.4	Other Vanadium oxides.....	20
3.2	Vanadates.....	21
3.3	Vanadium Phosphates .....	28
3.4	Sulphur-based Vanadium compounds .....	29
<b>4</b>	<b>Prussian Blue Analogues.....</b>	<b>31</b>
<b>5</b>	<b>Others .....</b>	<b>35</b>
<b>6</b>	<b>Summary and Further Outlook .....</b>	<b>36</b>
<b>7</b>	<b>Bibliography.....</b>	<b>37</b>

# 1 Introduction

Aqueous Zinc ion batteries (AZIBs) consist of a Zn anode, a  $\text{Zn}^{2+}$  based electrolyte, a cathode and a separator. Zinc-ion batteries have been around since Volta et al first demonstrated the use of Zn in 1799<sup>1</sup> in what is now known as the voltaic pile. In 1859, Gaston Planté discovered the world's first rechargeable battery type: the lead-acid battery<sup>2</sup>. More than 150 years and several breakthroughs later, battery technology has revolutionised the world and continues to open new avenues like decentralised smart grids (fig 1).

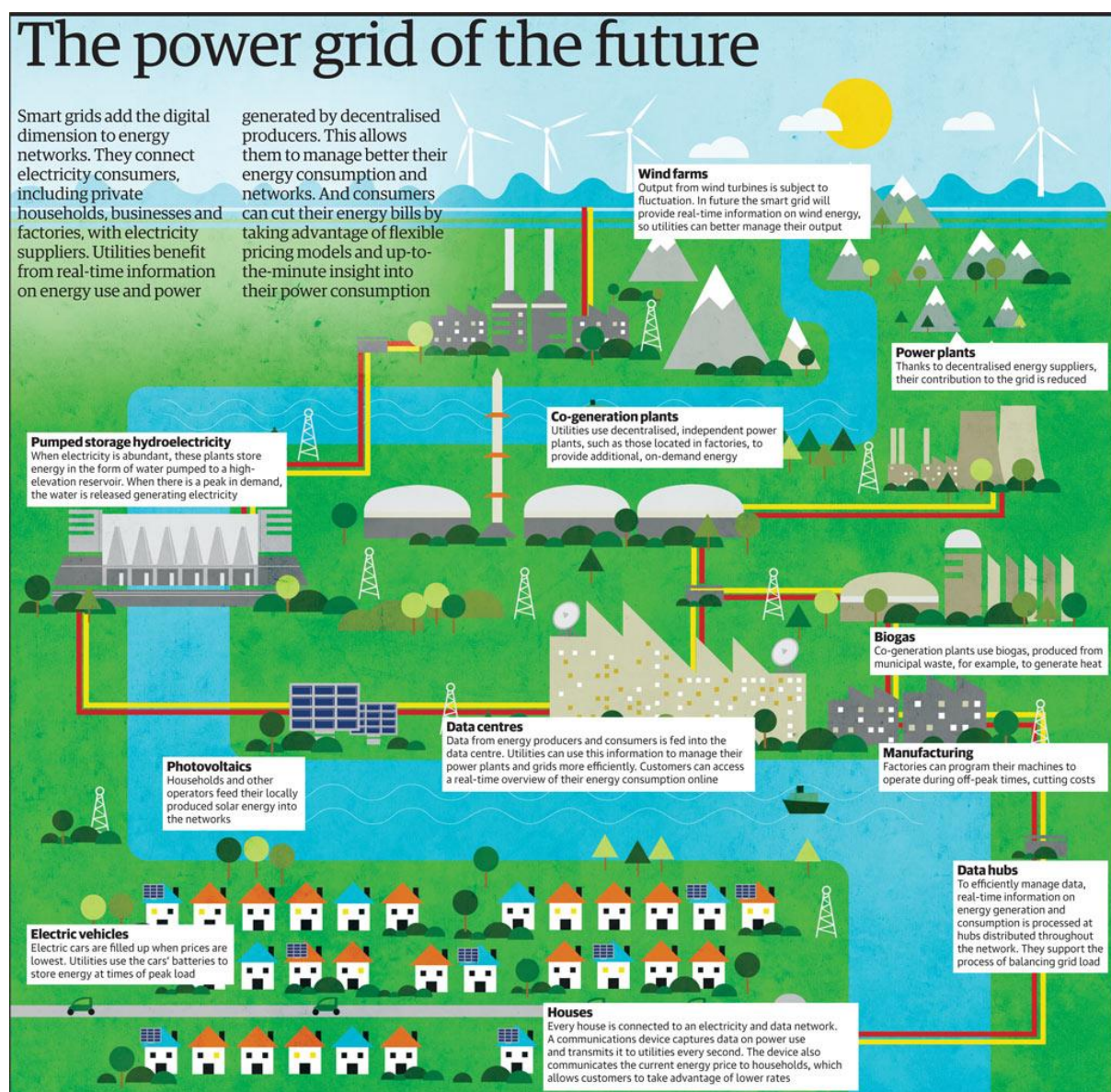


Figure 1 : Schematic illustration of a de-centralised energy grid mixing in several sources of energy managed via various energy storage systems<sup>101</sup>. Proposed to be the future of current grid systems

The use of Zn in battery chemistry has a long history and for good reason. It's an abundant, non-toxic element that is cheap to work with and has a low redox potential of  $-0.78\text{V}^3$  compared to the standard hydrogen electrode (SHE) potential, in addition to being a multivalent ion offering a high theoretical capacity of  $820\text{ mAhg}^{-1}$ .

The ratio of the number of  $\text{Zn}^{2+}$  produced during discharge to number of Zn atoms deposited back at the anode can be described as the coulombic efficiency. Presence of  $\text{OH}^-$  in alkaline electrolytes causes  $\text{Zn(OH)}_2$  or  $\text{ZnO}$  precipitation (fig 2) in primary alkaline zinc batteries, leading to sub-optimal Zn-deposition on the anode, returning low coulombic efficiencies and disappointing cycling ability<sup>4,5</sup>.

Mildly acidic aqueous electrolytes, on the other hand, allow for easier synthesis, are environment-friendly, non-flammable, non-explosive and can be easily recycled<sup>6</sup>. The ionic conductivity of aqueous electrolytes is about two orders of magnitude higher than those of non-aqueous electrolytes<sup>7,8,9</sup>, leading to faster reaction kinetics and potentially large power deliveries<sup>10,11</sup>. Reactions at the Zn anode are also greatly simplified where Zn exists as  $\text{Zn}^{2+}$  ion, allowing the much simpler, quicker and more efficient Zn stripping/ plating mechanism instead of the more lossy  $\text{Zn(OH)}_2$  reactions found in alkaline electrolytes, leading to minimal dendrite formation.

The divalent  $\text{Zn}^{2+}$  causes large electrostatic interactions with the cathode framework, resulting in gradual degradation of the electrode. The choice of electrolyte, while not specifically addressed in this review, is critical to ensuring good reversibility of the cathode and preventing unwanted side reactions<sup>12–14</sup>. Most cathodes in AZIBs store charge via an intercalation mechanism or a conversion reaction, with some employing a combination and others showing significant contribution from faradic pseudocapacitive behaviours. Upon discharge,  $\text{Zn}^{2+}$  ions typically rush into the cathode and are stored while the electrolyte is “re-filled” simultaneously by the anode via Zn stripping. The opposite takes place during charging.

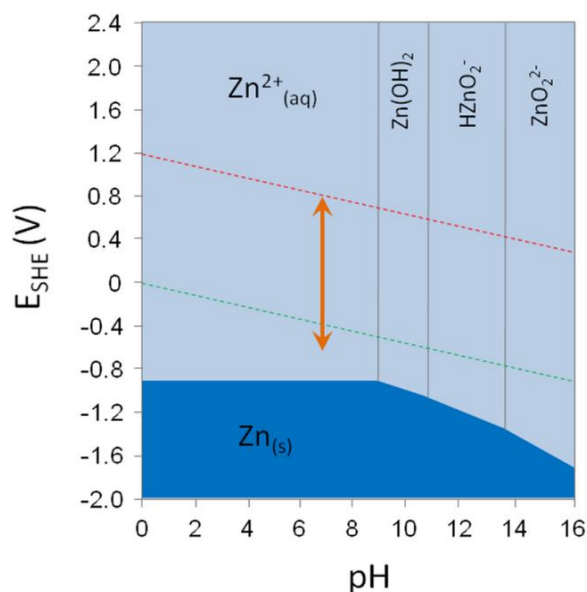


Figure 2 : Pourbaix Diagram for Zn where acidic environments result in the simpler  $\text{Zn}^{2+}$  ion compared to  $\text{Zn(OH)}_2$  in alkaline environments<sup>100</sup>

This review organises the electrochemical data of manganese-based (table 1), vanadium-based (tables 2-5), Prussian blue analogues (PBAs) (table 6) and other (table 7) materials in separate sections, with the following discussions outlining key findings in the field.

## 2 MnO<sub>2</sub>-based

Manganese oxides have been widely researched due to the variable oxidation states of manganese resulting in many crystal polymorphs.

Cathode	Electrolyte	Discharge Capacity (mAhg <sup>-1</sup> ) / Current Density (mA g <sup>-1</sup> )	Capacity Retention/ Charge Cycles/ Current Density (mA g <sup>-1</sup> )	Ref.
$\alpha$ -MnO <sub>2</sub>	1M ZnSO <sub>4</sub>	210 / 21	63% / 30 / 21	15,16
$\alpha$ -MnO <sub>2</sub>	2M ZnSO <sub>4</sub> + 0.1M MnSO <sub>4</sub>	285/103	92% / 5000 / 1540	17
$\beta$ -MnO <sub>2</sub>	1M ZnSO <sub>4</sub>	270/100	75% / 200 / 200	18
$\beta$ -MnO <sub>2</sub>	1M ZnSO <sub>4</sub> + 0.1M MnSO <sub>4</sub>	180/200	75%/200/200	18
$\beta$ -MnO <sub>2</sub>	3M Zn(CF <sub>3</sub> SO <sub>3</sub> ) <sub>2</sub> + 0.1M Mn(CF <sub>3</sub> SO <sub>3</sub> ) <sub>2</sub>	225/200	94% / 2000 / 2000	19
$\delta$ -MnO <sub>2</sub>	1 M ZnSO <sub>4</sub>	233/100	42% / 50 / 100	20
$\delta$ -MnO <sub>2</sub>	1M ZnSO <sub>4</sub> + 1M MnSO <sub>4</sub>	233/100	54% / 50 / 100	21
$\delta$ -MnO <sub>2</sub>	1 M ZnSO <sub>4</sub>	252/83	44% / 100/ 80	22,23
$\gamma$ -MnO <sub>2</sub> -graphene	5M ZnSO <sub>4</sub> + 1M MnSO <sub>4</sub>	301/500 and 95.8/10000	64% / 300 / 10000	24
$\gamma$ -MnO <sub>2</sub>	1M ZnSO <sub>4</sub> + 0.2M MnSO <sub>4</sub>	147/500	5% / 300 / 10000	25
Mn <sub>3</sub> O <sub>4</sub>	2M ZnSO <sub>4</sub>	232/200	72% / 265 / 500	26
SSWM@Mn <sub>3</sub> O <sub>4</sub>	2M ZnSO <sub>4</sub> + 0.1M MnSO <sub>4</sub>	296/100	~100% / 500 / 500	27
PANI-MnO <sub>2</sub>	2M ZnSO <sub>4</sub> + 0.1M MnSO <sub>4</sub>	280/200	~80% / 5000 / 2000	28
ZnMn <sub>2</sub> O <sub>4</sub> /C	3M Zn(CF <sub>3</sub> SO <sub>3</sub> ) <sub>2</sub>	150/50	94% / 500 / 500	29
ZnMn <sub>2</sub> O <sub>4</sub>	1M ZnSO <sub>4</sub> + 0.05M MnSO <sub>4</sub>	218/100	49% / 300 / 100	30

V-doped MnO <sub>2</sub>	1M ZnSO <sub>4</sub>	266/66	53% / 100 / 66	31
--------------------------	----------------------	--------	----------------	----

Table 1 : Electrochemical performance of MnO<sub>2</sub> based cathodes in recent research in AZIBs

## 2.1 $\alpha$ -MnO<sub>2</sub>

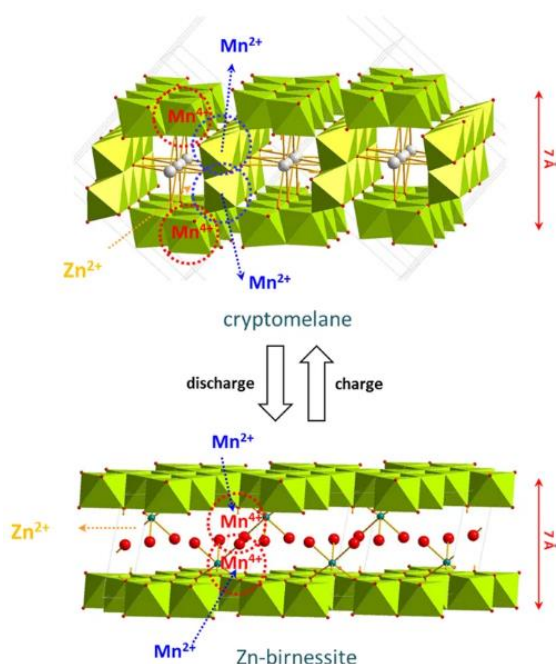


Figure 3 : Schematic illustration of Zn intercalation into  $\alpha$ -MnO<sub>2</sub>, leading to a structural change to Zn-birnessite and Mn<sup>2+</sup> dissolution<sup>26</sup>

Zn-insertion, where Mn<sup>4+</sup> in the cathode is reduced to Mn<sup>3+</sup> which disproportionates into Mn<sup>4+</sup>(s) and Mn<sup>2+</sup>(aq) which dissolves into the electrolyte. Removing the cathode from the electrolyte after discharge and placing into a fresh cell without the dissolved Mn<sup>2+</sup> leads to greatly reduced electrochemical reactivity, showing that the Mn<sup>2+</sup> must be reabsorbed upon charging. This dissolution, however, leads to less than ideal discharge capacities and rapid capacity fading due to structural stress<sup>17</sup>.

The dissolution of Mn<sup>2+</sup> can be largely mitigated by introducing Mn<sup>2+</sup> into the aqueous electrolyte, as done by Pan et al<sup>17</sup> via the addition of MnSO<sub>4</sub> into a ZnSO<sub>4</sub> aqueous electrolyte (fig 4). The pre-added Mn<sup>2+</sup> saturates the electrolyte, preventing further dissolution from the cathode itself. This results in a higher discharge capacity and superior capacity retention. Pan et al<sup>17</sup> also found, via XRD,

$\alpha$ -MnO<sub>2</sub> has been one of the most widely researched cathode materials for AZIBs. The basic building block of  $\alpha$ -MnO<sub>2</sub> are MO<sub>6</sub> octahedra, which come together to form 2x2 tunnels. The structure is stabilised by a small number of cations such as K<sup>+</sup> or Ba<sup>2+</sup> in the tunnels<sup>32</sup>, leading to large electrostatic interactions, especially with divalent Zn<sup>2+</sup> ions<sup>33</sup>.

Hao et al<sup>26</sup>, showed, via TEM analysis and later comparison using XRD, that the tunnelled  $\alpha$ -MnO<sub>2</sub> undergoes a reversible phase transformation to the layered Zn-birnessite ZnMn<sub>3</sub>O<sub>7</sub>·3H<sub>2</sub>O structure upon discharge (fig 3), confirming earlier reports<sup>15</sup>. Alfaruqi et al<sup>25</sup> proposed that the dissolution of Mn<sup>2+</sup> is related to the formation of Mn<sup>2+</sup> phases upon

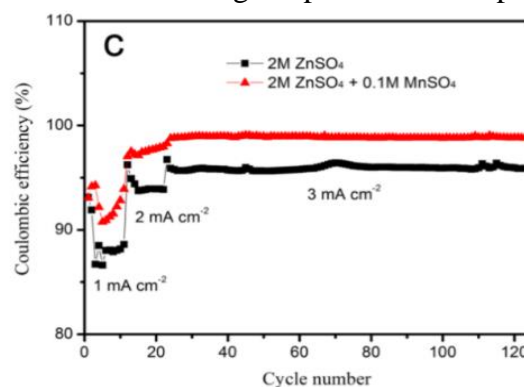


Figure 4 : Zn stripping/plating efficiency at the Zn anode with and without Mn<sup>2+</sup> pre-addition<sup>17</sup> with MnO<sub>2</sub> cathode



TEM and STEM-EDS, that the discharge product is not the previously reported Zn-birnessite but instead MnOOH. It is postulated that this product emerges via a conversion reaction ( $\text{MnO}_2 + \text{H}^+ + \text{e}^- \leftrightarrow \text{MnOOH}$ ) instead of previously reported intercalation.

## 2.2 $\beta\text{-MnO}_2$

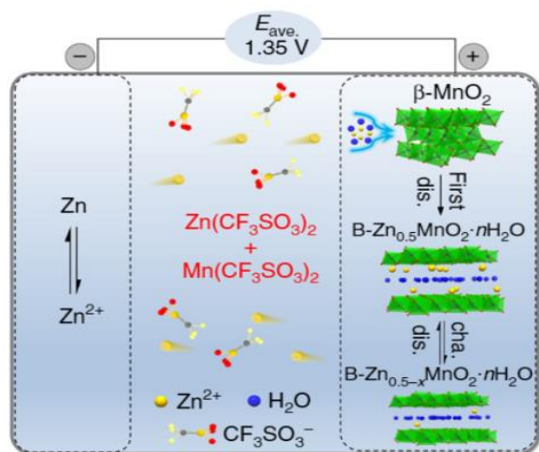


Figure 5 : Schematic illustration showing transformation of  $\beta\text{-MnO}_2$  to Zn-buserite upon the first discharge and reversible intercalation of Zn into the new phase upon further cycling using  $\text{Zn}(\text{CF}_3\text{SO}_3)_2 + \text{Mn}(\text{CF}_3\text{SO}_3)_2$  electrolyte<sup>18</sup>

discharge cycle; subsequent cycles show a Zn-intercalation mechanism with this new Zn-buserite phase (fig 5), using a  $\text{CF}_3\text{SO}_3$  based electrolyte. This phenomenon is common for  $\alpha$ ,  $\beta$  and  $\gamma\text{-MnO}_2$  cathodes (figs 6 & 7). On the other hand, Islam et al<sup>18</sup> show formation of a spinel  $\text{ZnMn}_2\text{O}_4$  phase in the electrode along with  $\text{ZnSO}_4 \cdot 3\text{Zn}(\text{OH})_2 \cdot 5\text{H}_2\text{O}$  on the surface of the electrode due to the precipitation of Zn salt from the electrolyte<sup>36</sup>. The surface phase, however, is not shown to negatively affect electrochemical performance<sup>17</sup>. This disagreement

$\beta\text{-MnO}_2$  forms  $1 \times 1$  tunnels of  $\text{MnO}_6$  octahedra with a tunnel width of  $2.3 \text{ \AA}$ , which is the smallest among  $\text{MnO}_2$  polymorphs<sup>34</sup>.

Zhang<sup>19</sup> et al found that the nano-structured version shows better electrochemical performance owing to the increased surface area and greater contact between electrolyte and cathode whereas the bulk version shows little to no reactivity.<sup>34</sup> Exact crystal orientation and the exposure of different planes to the electrolyte has been shown to affect battery performance<sup>35–37</sup>. Islam et al<sup>18</sup> synthesized  $\beta\text{-MnO}_2$  with exposed 101 planes, showing a complete phase transformation to Zn-buserite by the  $\sim 10^{\text{th}}$

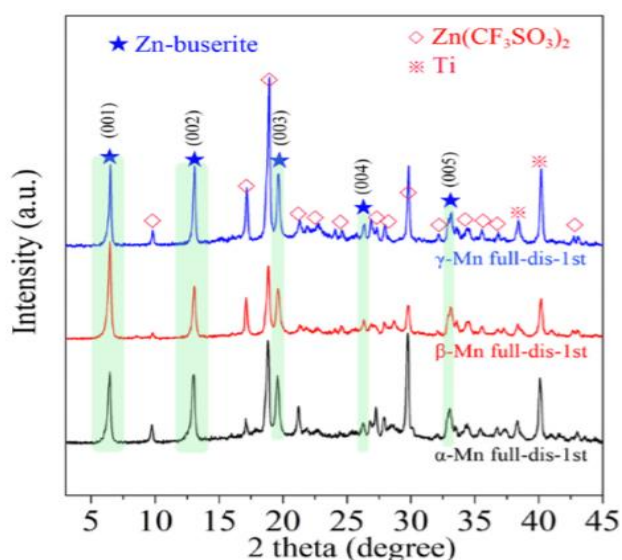


Figure 6 : XRD patterns of  $\alpha$ ,  $\beta$  and  $\gamma\text{-MnO}_2$  cathodes after the first discharge, showing a common transformation to Zn-buserite<sup>20</sup> in AZIBs

between papers suggests that the reaction mechanism at the electrode is greatly affected by the microstructure of the electrode as well as the electrolyte being employed.

The pre-addition of  $\text{Mn}^{2+}$  ions shows lower initial discharge capacity but improved cycling ability, agreeing with previous discussions. The use of  $\text{CF}_3\text{SO}_3^-$  anions<sup>19</sup> shows both a higher discharge capacity and better cycling ability than the smaller  $\text{SO}_4^{2-}$  anion due to a reduced solvation effect<sup>30</sup>.

### 2.3 $\delta\text{-MnO}_2$

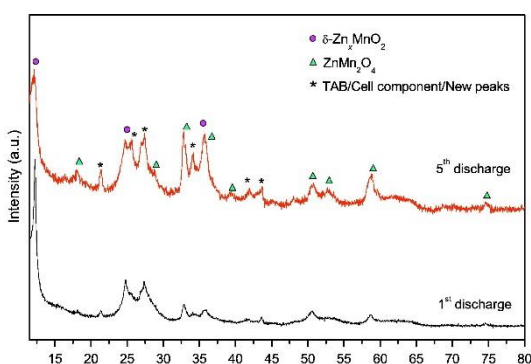


Figure 8 : Phase transformation of  $\delta\text{-MnO}_2$  to Spinel  $\text{ZnMn}_2\text{O}_4$  as it occurs on the 5th discharge<sup>21</sup> in 1M  $\text{ZnSO}_4$  + 1M  $\text{MnSO}_4$  electrolyte

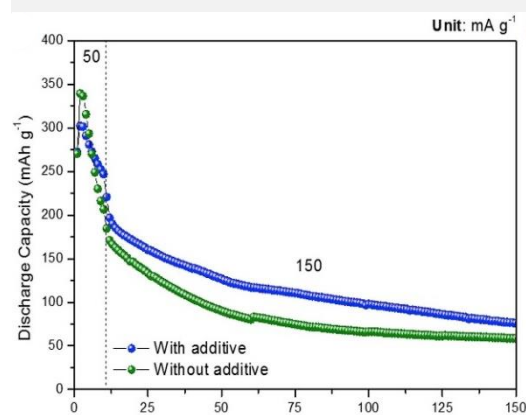


Figure 9 : Cycling performance of  $\delta\text{-MnO}_2$  with  $\text{MnSO}_4$  and without  $\text{MnSO}_4$  addition in 1M  $\text{ZnSO}_4$  electrolyte<sup>20</sup>

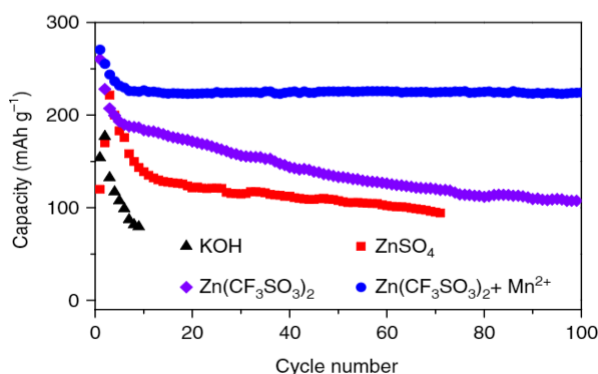


Figure 7 : Discharge capacity over 100 cycles with a  $\beta\text{-MnO}_2/\text{Zn}$  battery with 45wt.% KOH (black), 3M  $\text{ZnSO}_4$  (red), 3M  $\text{Zn}(\text{CF}_3\text{SO}_3)_2$  (purple) and 3M  $\text{Zn}(\text{CF}_3\text{SO}_3)_2$  + 0.1M  $\text{Mn}(\text{CF}_3\text{SO}_3)_2$  (blue)<sup>18</sup>

$\delta\text{-MnO}_2$  forms a 2D layered birnessite<sup>21</sup> structure with an interlayer distance of  $7\text{\AA}$ , consisting of edge-sharing  $\text{MnO}_6$  octahedra. In 2015, Alfaruqi et al<sup>21</sup> found via XRD analysis that, upon discharge, the layered  $\delta\text{-MnO}_2$  undergoes a reversible phase transformation to spinel  $\text{ZnMn}_2\text{O}_4$  (figs 8 & 10) through an intermediate layered  $\delta\text{-Zn}_x\text{Mn}_2\text{O}_4$ . No evidence of other irreversible phases is found indicating that the electrode relies solely on Zn-intercalation for charge storage, contrary to the tunnelled polymorphs of  $\text{MnO}_2$ . Later in 2018, Alfaruqi et al<sup>20</sup> show, via XRD, that the layered  $\delta\text{-MnO}_2$  maintains its layered structure along with the new Zn-inserted phase during initial cycles but eventually transforms irreversibly into a spinel phase, leading to rapid capacity fading. Additionally, they show that the addition of  $\text{MnSO}_4$  into the electrolyte has little improvement in electrochemical performance (fig 9), indicating that electrolyte optimisation is crucial for electrochemical performance.



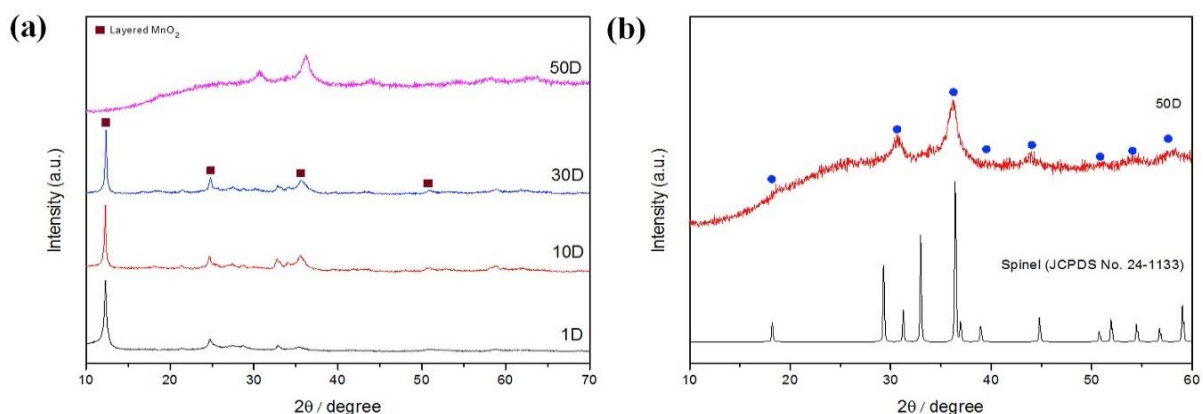


Figure 10 : XRD comparison showing (a) gradual irreversible transformation of  $\delta$ -MnO<sub>2</sub> cathode from layered to spinel ZnMn<sub>2</sub>O<sub>4</sub> over 50 charge/ discharge cycles and (b) comparison of the electrode obtained after the 50th cycle against reference spinel ZnMn<sub>2</sub>O<sub>4</sub> showing good match<sup>25</sup> in 1M ZnSO<sub>4</sub> + 1M MnSO<sub>4</sub> electrolyte

## 2.4 $\gamma$ -MnO<sub>2</sub>

$\gamma$ -MnO<sub>2</sub> contains an arrangement of 1x1 (2.3×2.3Å) and 1x2 (2.3×4.6Å) tunnels and exists as a hybrid of R-MnO<sub>2</sub> and  $\beta$ -MnO<sub>2</sub> structures.

Alfaruqi et al<sup>25</sup> proposed that Zn-intercalation into  $\gamma$ -MnO<sub>2</sub> leads to a structural transformation into the spinel phase<sup>20,24</sup> ZnMn<sub>2</sub>O<sub>4</sub> (fig 12) with further Zn-intercalation into the remaining  $\gamma$ -MnO<sub>2</sub> leading to an expansion of the 1x2 tunnels into the larger  $\gamma$ -Zn<sub>x</sub>MnO<sub>2</sub> phase which eventually gives way to the

layered Zn<sub>y</sub>MnO<sub>2</sub> upon continued Zn-intercalation. Not all the inserted Zn is extracted back out during charging, leading to capacity loss, a common problem among other cathode materials, particularly for Zn poisoning in Prussian blue cathodes<sup>38–41</sup>.

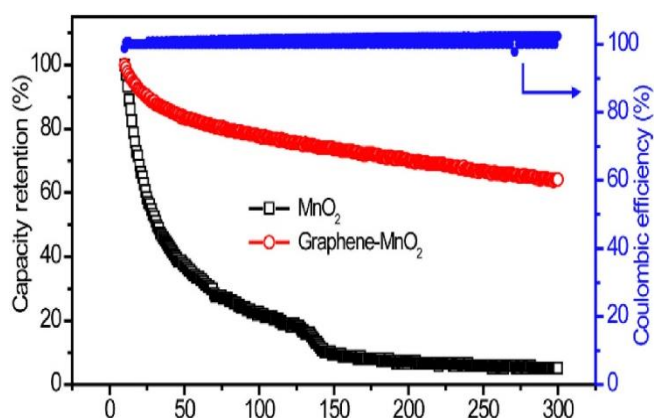


Figure 11 : Capacity retention over 300 cycles with  $\gamma$ -MnO<sub>2</sub> and  $\gamma$ -MnO<sub>2</sub>-graphene cathodes at a current density of 500 mA g<sup>-1</sup> in 2M ZnSO<sub>4</sub> + 0.4M MnSO<sub>4</sub> aqueous electrolyte<sup>24</sup>

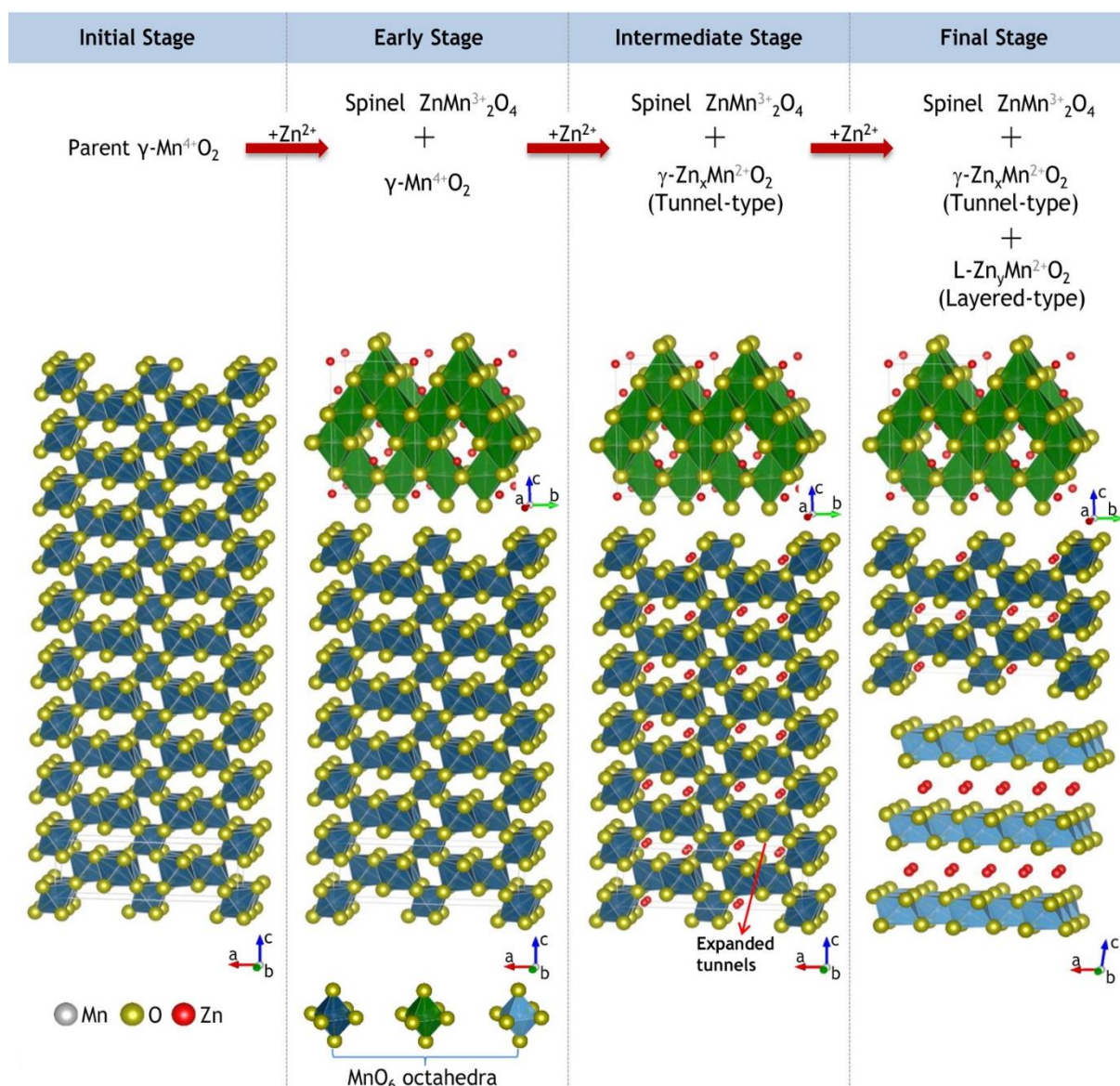


Figure 12 : Schematic illustration of the phase transformation from layered  $\gamma\text{-MnO}_2$  to spinel  $\text{ZnMn}_2\text{O}_4$  + layered  $\text{Zn}_y\text{MnO}_2$  as discharge process continues from left to right in 1M  $\text{ZnSO}_4$  + 0.2M  $\text{MnSO}_4$  electrolyte<sup>25</sup>

This capacity loss can be alleviated by improving structural stability. Wang et al<sup>24</sup> synthesised a graphene- $\gamma\text{-MnO}_2$ , owing to the higher ionic conductivity of graphene as well as structural support for the  $\text{MnO}_2$ , with discharge capacities more than twice as high, at the same current, as the bare  $\gamma\text{-MnO}_2$ , markedly superior cycling performance and vastly improved rate capability (fig 11).

## 2.5 Mn<sub>3</sub>O<sub>4</sub>

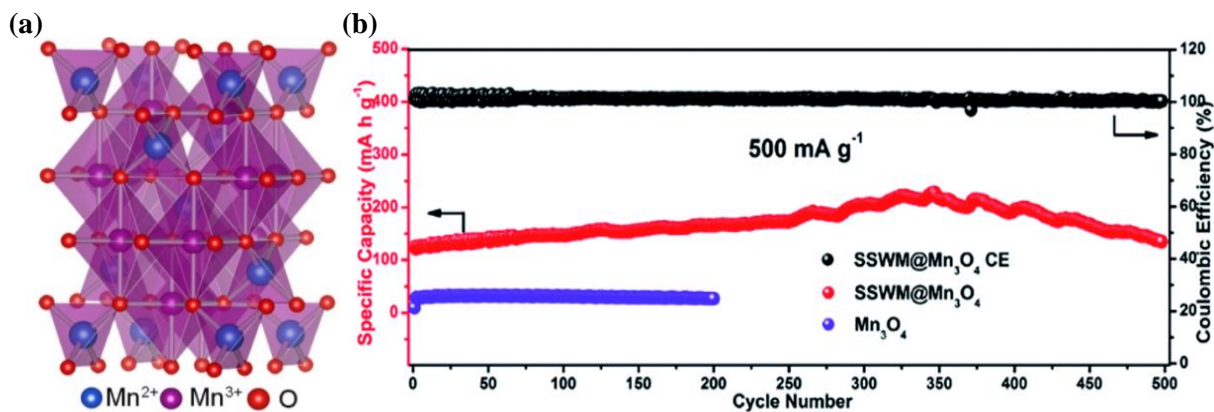


Figure 13 : (a) Schematic illustration of the Mn<sub>3</sub>O<sub>4</sub> structure<sup>26</sup> and (b) discharge capacity and coulombic efficiency over 500 cycles<sup>27</sup> for Mn<sub>3</sub>O<sub>4</sub> and SSWM@Mn<sub>3</sub>O<sub>4</sub> in aqueous 2M ZnSO<sub>4</sub> + 0.1M MnSO<sub>4</sub>

Mn<sub>3</sub>O<sub>4</sub> adopts a spinel structure (fig 13a) where Mn<sup>2+</sup> and Mn<sup>3+</sup> reside in the tetragonal and octahedral holes, respectively, in a cubic close packed array of oxygen atoms.

Hao et al<sup>26</sup> describe the mechanism as follows: upon first charge a new phase of Mn<sub>5</sub>O<sub>8</sub> and cation-free birnessite MnO<sub>2</sub>·xH<sub>2</sub>O occurs in the pristine Mn<sub>3</sub>O<sub>4</sub> material. Subsequent discharging show Zn-birnessite emergence, which upon further cycling becomes irreversible. Upon discharge, reversible phase emergence of MnOOH and Zn<sub>4</sub>(OH)<sub>6</sub>SO<sub>4</sub>·5H<sub>2</sub>O is seen (figs 14 & 15).

These two products are associated with the pH evolution of the electrolyte<sup>42</sup>. The generation of MnOOH occurs due to H<sup>+</sup> conversion reaction during discharge which causes the pH to rise<sup>27</sup>, leading to the generation of Zn<sub>4</sub>(OH)<sub>6</sub>SO<sub>4</sub>·5H<sub>2</sub>O. This is confirmed by Zhu et al<sup>27</sup> where the appearance of

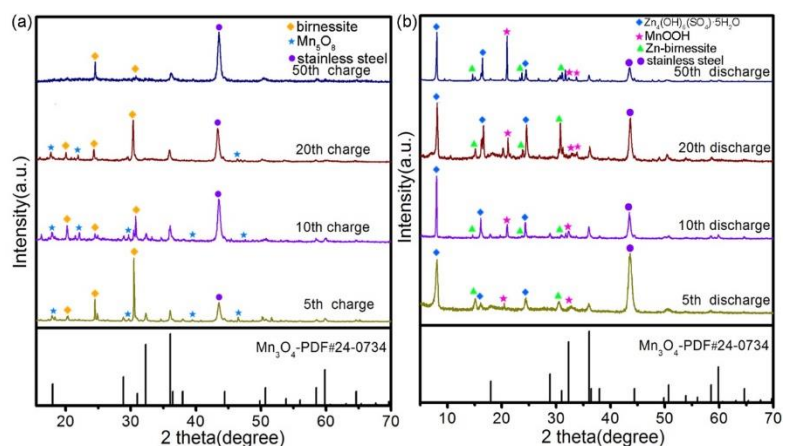


Figure 14 : XRD patterns of Mn<sub>3</sub>O<sub>4</sub> cathode showing gradual phase transformation during 50 charge/ discharge cycles in 2M ZnSO<sub>4</sub> electrolyte<sup>26</sup>

Zn<sub>4</sub>(OH)<sub>6</sub>SO<sub>4</sub>·5H<sub>2</sub>O is detected during the first discharge, along with MnOOH. ZnSO<sub>4</sub> and H<sub>2</sub>O are proposed to react with the OH<sup>-</sup> ions from MnOOH to form Zn<sub>4</sub>(OH)<sub>6</sub>SO<sub>4</sub>·5H<sub>2</sub>O.



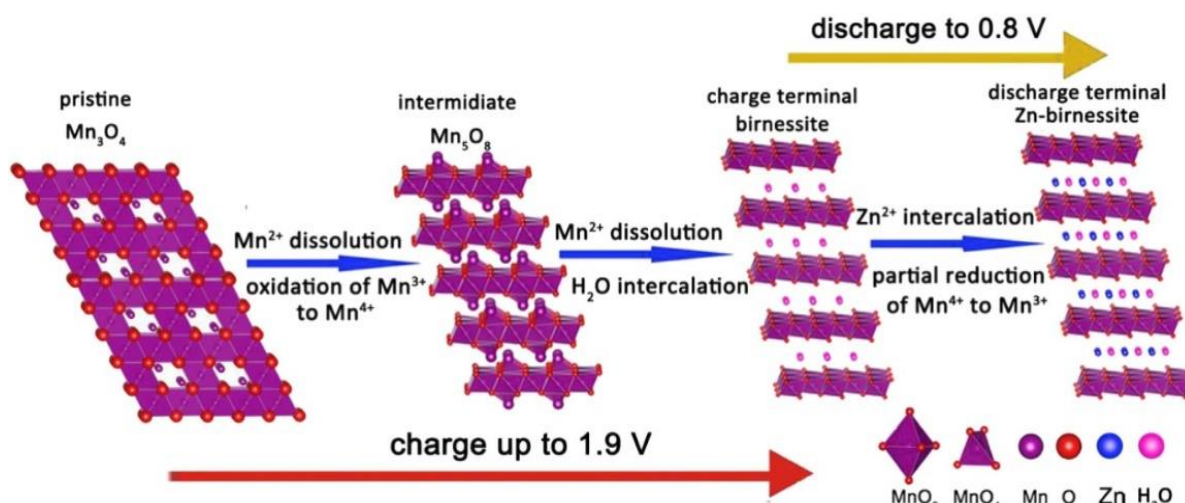


Figure 15 : Schematic illustration of  $\text{Mn}^{2+}$  dissolution,  $\text{H}_2\text{O}$  intercalation and subsequent discharge in  $\text{Mn}_3\text{O}_4$  in 2M  $\text{ZnSO}_4$  electrolyte<sup>26</sup>

This gradual change in morphology is attributed to the increase in discharge capacity experienced during the initial cycles. This “activation” is much more pronounced in Zhu et al’s work<sup>27</sup> where a 3D stainless steel mesh (SSWM) provides structural stability, prolonging this morphological conversion. The continual phase transformation, nonetheless, causes stress in the electrode. The nanoflower composite shows better discharge capacity, capacity retention and rate capability than the bare  $\text{Mn}_3\text{O}_4$ , attributing most of the performance to the existence of the nanoflowers on the SSWM (fig 16), which reduces diffusion path and facilitates infiltration, provides a stable structure for support and higher electrical conductivity than the bare  $\text{Mn}_3\text{O}_4$ , leading to the better performance (fig 13b).

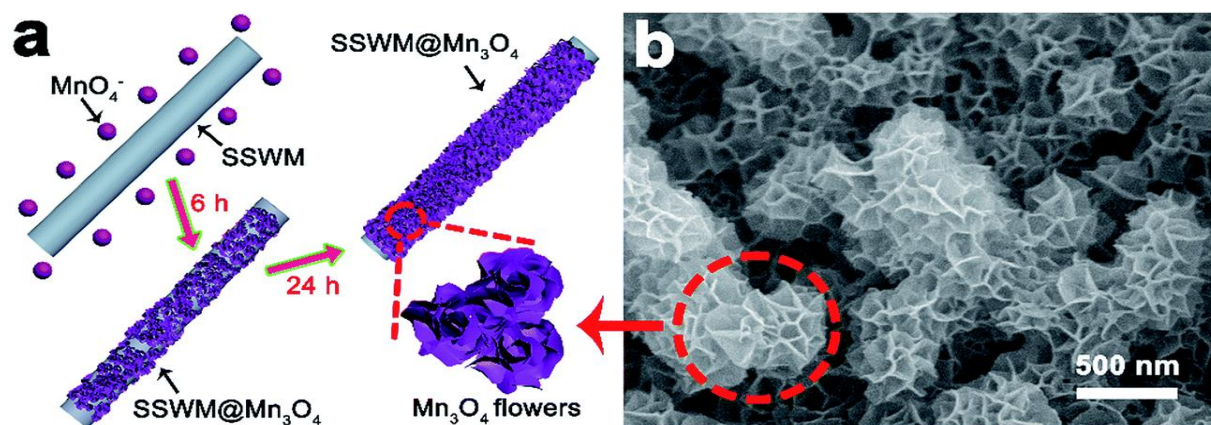


Figure 16 : (a) Schematic illustration and (b) SEM image of the  $\text{Mn}_3\text{O}_4$  nanoflowers on a 3D stainless steel mesh<sup>27</sup>

## 2.6 Other Mn-based Cathodes

Huang et al<sup>28</sup> synthesized PANI-intercalated nano-layered  $\text{MnO}_2$  where the polyaniline structure supports the  $\text{MnO}_2$  layered structure (fig 17) and prevents collapse during repeated cycling, leading to remarkable cycling performance.

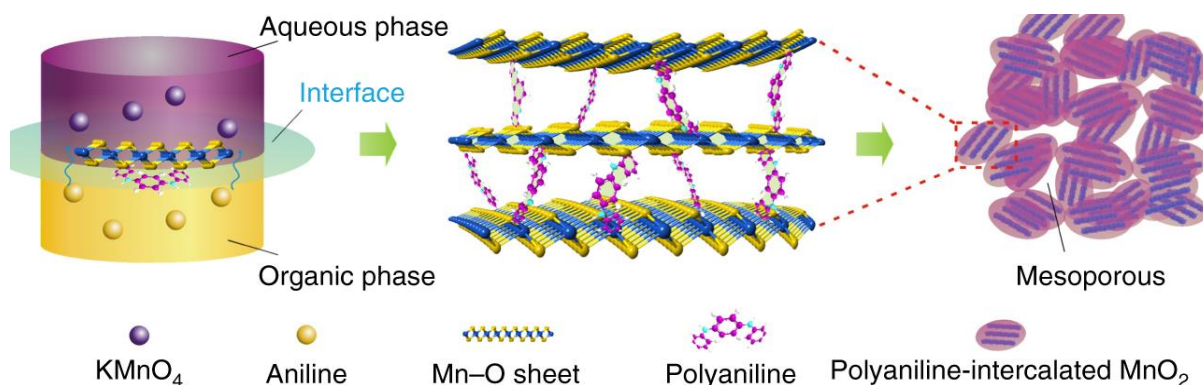


Figure 17 : Schematic illustration of polyaniline (PANI)-intercalated<sup>28</sup>  $\text{MnO}_2$

The intercalation mechanism in PANI- $\text{MnO}_2$  involves a  $\text{H}^+$  conversion reaction where the insertion of  $\text{H}^+$  ions leaves behind an excess of  $\text{OH}^-$  ions in the electrolyte, which reacts with  $\text{ZnSO}_4$  to produce  $\text{Zn}_4(\text{OH})_6\text{SO}_4 \cdot 5\text{H}_2\text{O}$  on the electrode surface, as previously reported by Pan et al<sup>17</sup>. The consumption of  $\text{OH}^-$  in the electrolyte to form  $\text{Zn}_4(\text{OH})_6\text{SO}_4 \cdot 5\text{H}_2\text{O}$  may, in fact, be beneficial to cycling as it maintains electrolyte pH. However, Zhang et al<sup>29</sup> show that the spinel  $\text{ZnMnO}_2$  cathode relies solely on  $\text{Zn}^{2+}$  intercalation with no  $\text{H}^+$  insertion occurring, confirming this via the use of a non-aqueous  $\text{Zn}(\text{CF}_3\text{SO}_3)_2$  electrolyte where a capacity of  $\sim 90 \text{ mAh g}^{-1}$  was achieved compared to no electrochemical activity in an aqueous non-Zn

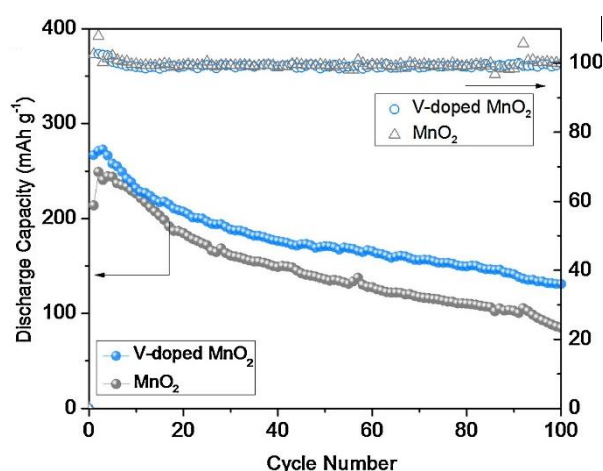


Figure 18 : Capacity retention over 100 cycles of bare  $\text{MnO}_2$  and V-doped  $\text{MnO}_2$  at a current density of  $66 \text{ mAh g}^{-1}$  in aqueous  $1\text{M ZnSO}_4$ <sup>31</sup>

electrolyte. Moreover, no  $\text{MnOOH}$  formation was detected using FTIR spectra. It is noted that Huang et al<sup>28</sup> use excess Zn anode, to exclude the effect of Zn-fading for the extended cycling test. However, given that Zn stripping/ plating at the anodes typically have  $\sim 100\%$  coulombic efficiency in AZIBs, these results should still be valid.

Zhang et al<sup>29</sup> have shown that carbon-composite cation-deficient spinel  $\text{ZnMn}_{1.86}\text{Y}_{0.14}\text{O}_4$ , with higher vacancies than



bare  $\text{ZnMn}_{1.98}\text{Y}_{0.02}\text{O}_4$ , where Y = vacancy, makes multivalent guest cation insertion easier. In comparison to Wu et al<sup>30</sup> who synthesized bare spinel  $\text{ZnMn}_2\text{O}_4$ , resulting in lower capacity retention, as seen in table 1.

Alfaruqi et al<sup>31</sup> show that vanadium doping  $\text{MnO}_2$  produces  $\text{V}_{0.05}\text{MnO}_2$  with a +3.75-oxidation state on the Mn instead of the +4 in bare  $\text{MnO}_2$  electrode, leading to reduced electrostatic repulsion. increased electrode surface area and higher electronic conductivity. The V-doped  $\text{MnO}_2$  shows larger pore volumes in the mesoporous structure leading to easier guest ion insertion and better cycling ability (fig 18). The capacity loss is attributed to irreversible Zn intercalation.

### 3 Vanadium-based

The variable oxidation states (+5, +4, +3 and +2) that vanadium can occupy leads to a large variety of compounds with varying electrochemical properties and charge-storage mechanisms. This review organises these compounds into vanadium oxides, vanadates, vanadium phosphates and vanadium sulphides.

#### 3.1 Vanadium Oxides

Cathode	Electrolyte	Discharge Capacity (mAhg <sup>-1</sup> ) / Current Density (mA g <sup>-1</sup> )	Capacity Retention/ Charge Cycles/ Current Density (mA g <sup>-1</sup> )	Ref.
<b>V<sub>2</sub>O<sub>5</sub></b>	3 M Zn(CF <sub>3</sub> SO <sub>3</sub> ) <sub>2</sub>	319/20	81%/500/588	43
<b>V<sub>2</sub>O<sub>5</sub></b>	3 M ZnSO <sub>4</sub>	275/588	27%/100/588	44
<b>V<sub>2</sub>O<sub>5</sub></b>	21M LiTFSI + 1M Zn(CF <sub>3</sub> SO <sub>3</sub> ) <sub>2</sub>	238/50	80%/2000/2000	45
<b>VO<sub>2</sub></b>	1 M ZnSO <sub>4</sub>	325.6/50	86%/5000/3000	46
<b>VO<sub>2</sub></b>	3M Zn(CF <sub>3</sub> SO <sub>3</sub> ) <sub>2</sub>	357/100 and 171/51200	91.2%/300/2000	47
<b>VO<sub>2</sub></b>	3M Zn(CF <sub>3</sub> SO <sub>3</sub> ) <sub>2</sub>	274/100	79%/10000/10000	48
<b>VO<sub>2</sub>/rGO</b>	1 M ZnSO <sub>4</sub>	365/50	80%/200/50	49
<b>H<sub>2</sub>V<sub>3</sub>O<sub>8</sub></b>	3M Zn(CF <sub>3</sub> SO <sub>3</sub> ) <sub>2</sub>	423.8/100 and 113.9/5000	94.3%/1000/5000	50
<b>V<sub>6</sub>O<sub>13</sub>.nH<sub>2</sub>O</b>	3M Zn(CF <sub>3</sub> SO <sub>3</sub> ) <sub>2</sub>	395/100	87%/1000/5000	51
<b>V<sub>10</sub>O<sub>24</sub>.12H<sub>2</sub>O</b>	3 M Zn(CF <sub>3</sub> SO <sub>3</sub> ) <sub>2</sub>	164.5/200	80.1%/3000/10000	52
<b>V<sub>2</sub>O<sub>5</sub>.nH<sub>2</sub>O/graphene</b>	3 M Zn(CF <sub>3</sub> SO <sub>3</sub> ) <sub>2</sub>	319/15000	71%/900/3000	53

Table 2 : Electrochemical performance of vanadium oxides in recent research in AZIBs

### 3.1.1 V<sub>2</sub>O<sub>5</sub>

V<sub>2</sub>O<sub>5</sub> is a layered orthorhombic oxide<sup>43</sup> (fig 19). The layers are often held up by metal ions or water molecules within the structure with a larger interlayer spacing of 12.6 Å.

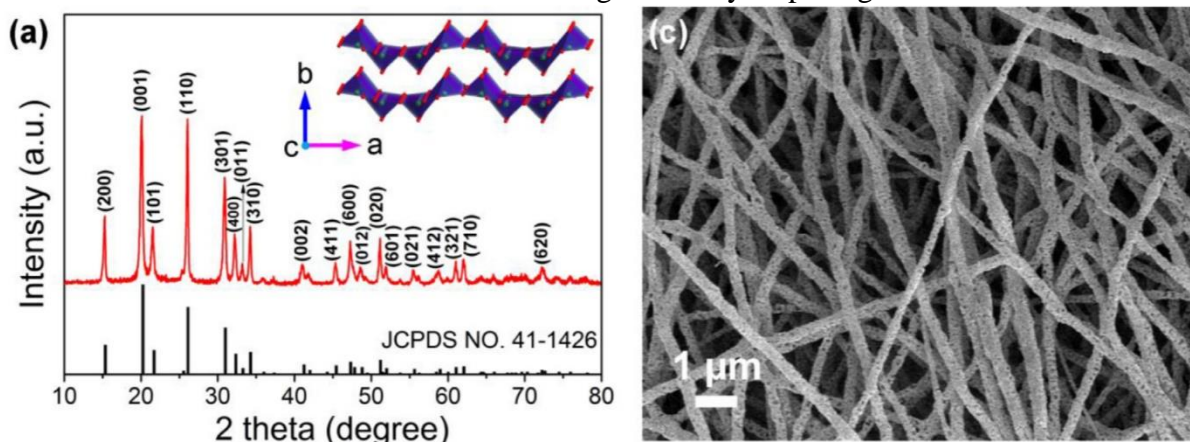


Figure 19 : (a) XRD pattern and (c) SEM image of V<sub>2</sub>O<sub>5</sub> nanofibers<sup>43</sup>

Chen et al<sup>43</sup> observed a phase transition from V<sub>2</sub>O<sub>5</sub> to Zinc-pyrovanadate (ZPV) Zn<sub>3+x</sub>(OH)<sub>2</sub>V<sub>2</sub>O<sub>7</sub>·2H<sub>2</sub>O upon first discharge, with subsequent cycling showing Zinc insertion/extraction from ZPV<sup>54</sup> (fig 20). ZPV has an open structure of ZnO<sub>6</sub> octahedral layers separated by double VO<sub>4</sub> tetrahedra, with water molecules randomly found in the large cavities. ZPV was in fact reported as a high-performance cathode for ZIBs by Xia et al<sup>54</sup>. The structure is extremely stable upon cycling. After 100 cycles, the formation of nanoflakes is observed by Chen et al<sup>43,46</sup>, which has been shown to facilitate Zn<sup>2+</sup> insertion/ extraction<sup>29</sup>

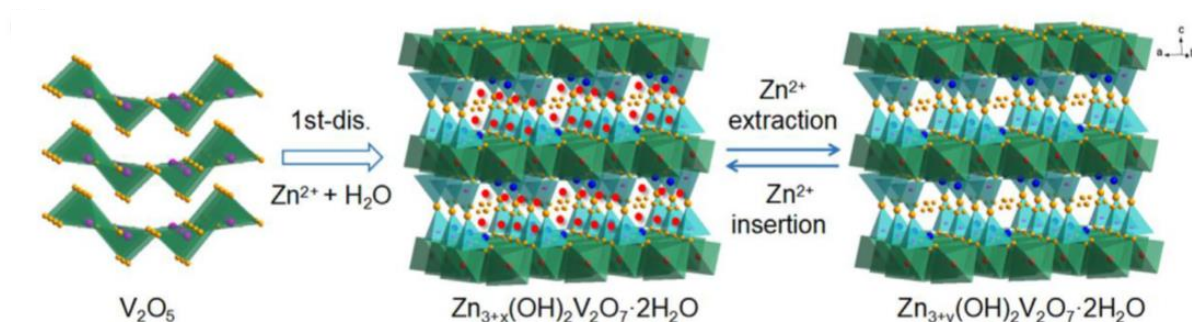


Figure 20 : Schematic illustration of the phase change upon charging/ discharging in V<sub>2</sub>O<sub>5</sub> in 3 M Zn(CF<sub>3</sub>SO<sub>3</sub>)<sub>2</sub> electrolyte<sup>43</sup>

The use of 3M ZnSO<sub>4</sub> electrolyte shows considerably worse electrochemical properties. Zhang et al<sup>44</sup> propose this is due to the bulky triflate anion CF<sub>3</sub>SO<sub>3</sub><sup>-</sup> and its better ionic conductivity, with a reduced solvation effect, compared to the SO<sub>4</sub><sup>2-</sup> ion.

Hu et al<sup>45</sup> showed the use of a water in salt electrolyte in a Li-Zn hybrid battery retards hydrogen and oxygen evolution at high voltages, facilitates ionic activity<sup>44</sup> and leads to better cycling ability (fig 21), with a V<sub>2</sub>O<sub>5</sub> cathode. A synergistic effect is seen where the

$\text{Zn}(\text{CF}_3\text{SO}_3)_2$  provides  $\text{Zn}^{2+}$  ions for stripping/ plating on the anode as well as (de)intercalation into the cathode along with  $\text{Li}^+$  ions. This has been reported by several other studies<sup>45,55–58</sup>.

In 2018, Zhang et al<sup>44</sup> demonstrated the use of bulk pre-intercalated  $\text{Zn-V}_2\text{O}_5$  with outstanding rate capability and cycling ability. A gradual increase in capacity is seen over the initial cycles with capacity stabilising over subsequent cycling due to the bulk electrode undergoing structural evolution to layered  $\text{Zn}_x\text{V}_2\text{O}_5 \cdot n\text{H}_2\text{O}$ , resulting in enlarged interlayer spacing from 4.4 Å to 13.4 Å, due to repeated co-insertion of  $\text{Zn}^{2+}$  and  $\text{H}_2\text{O}$ . The  $\text{H}_2\text{O}$  screens the electrostatic interactions between  $\text{Zn}^{2+}$  and electrode. The excellent rate capabilities are attributed to significant pseudocapacitive<sup>54,40</sup> effects (fig 22).

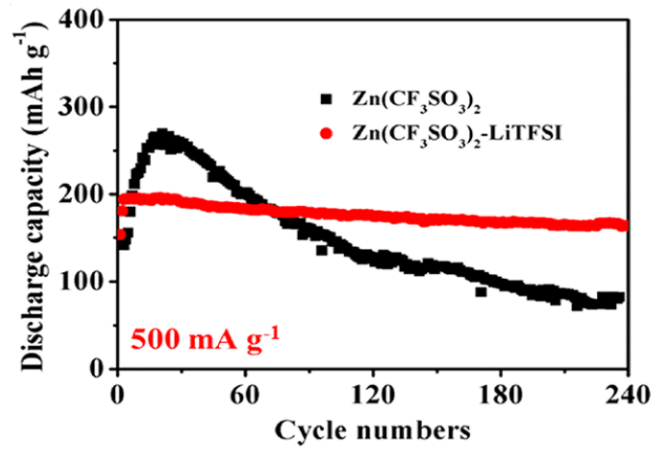


Figure 21 : Cycling performance of  $\text{V}_2\text{O}_5$  at  $500\text{mA g}^{-1}$  using a “water-in-salt”  $\text{LiC}_2\text{F}_6\text{NO}_4\text{S}_2$  (LiTFSI) electrolyte<sup>45</sup>

### 3.1.2 $\text{VO}_2(\text{B})$

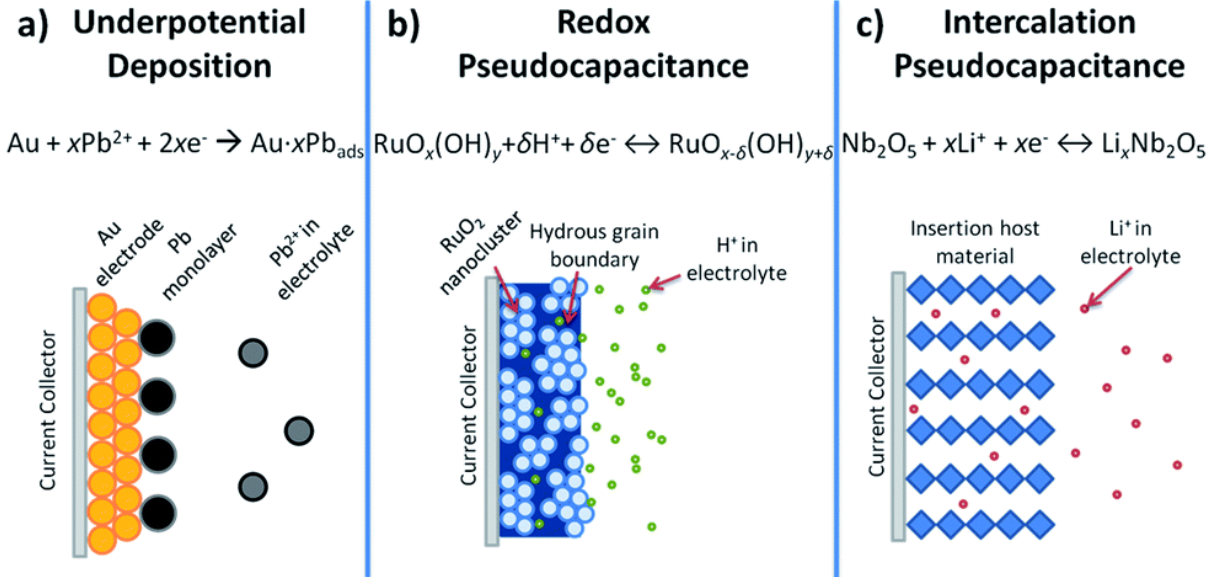


Figure 22 : Schematic illustration of three types of pseudocapacitive behaviour<sup>51</sup>  
 $\text{VO}_2$  has several polymorphs<sup>59</sup>;  $\text{VO}_2$  (A),  $\text{VO}_2$  (B),  $\text{VO}_2$  (M1) and  $\text{VO}_2$  (R), where M = monoclinic, R = rutile, B = monoclinic and A = tetragonal.  $\text{VO}_2(\text{B})$  is built from corner-edge sharing  $\text{VO}_6$  octahedra forming a tunnel like structure (fig 23), and it has been extensively studied. Chen et al<sup>46</sup> show reversible insertion/ extraction of  $\text{Zn}^{2+}$  into the  $\text{VO}_2(\text{B})$  cathode with minimal Zn residue left after the charging process and minimal volumetric change.

Ding et al<sup>47</sup> reported fantastic rate capabilities for the VO<sub>2</sub>(B) cathode in 2018 with a 3M Zn(CF<sub>3</sub>SO<sub>3</sub>)<sub>2</sub> electrolyte, using a large current density of 51.2 mA g<sup>-1</sup>. The unprecedented rate capabilities are attributed to a pseudocapacitive<sup>60,54,48</sup> behaviour (fig 22) and are thus not limited by solid solution diffusion. Little structural change is detected upon cycling. Wei et al<sup>48</sup>, however, reported an irreversible phase transition from VO<sub>2</sub>(B) (monoclinic) to bi-layered V<sub>2</sub>O<sub>5</sub>·nH<sub>2</sub>O during the initial cycle with subsequent cycling

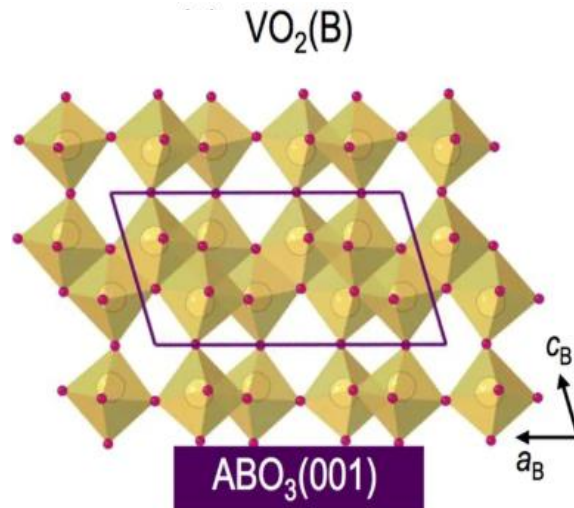


Figure 23 : Schematic illustration of VO<sub>2</sub>(B) structure<sup>59</sup>

using the new phase (fig 24), which has been shown as an excellent cathode material for AZIBs<sup>50</sup>, owing to the electrostatic shielding provided by the intercalated water molecules, reducing electrostatic interactions of Zn<sup>2+</sup> within the framework.

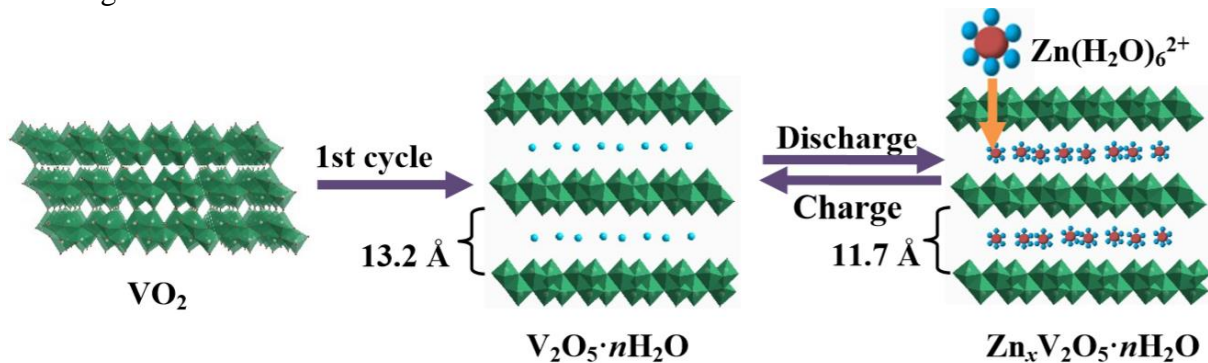


Figure 24 : Schematic illustration of the phase transformation from VO<sub>2</sub>(B) to V<sub>2</sub>O<sub>5</sub>·nH<sub>2</sub>O after the first cycle and then subsequent cycling in 3M Zn(CF<sub>3</sub>SO<sub>3</sub>)<sub>2</sub> electrolyte<sup>48</sup>



### 3.1.3 $V_3O_7 \cdot H_2O$ ( $H_2V_3O_8$ )

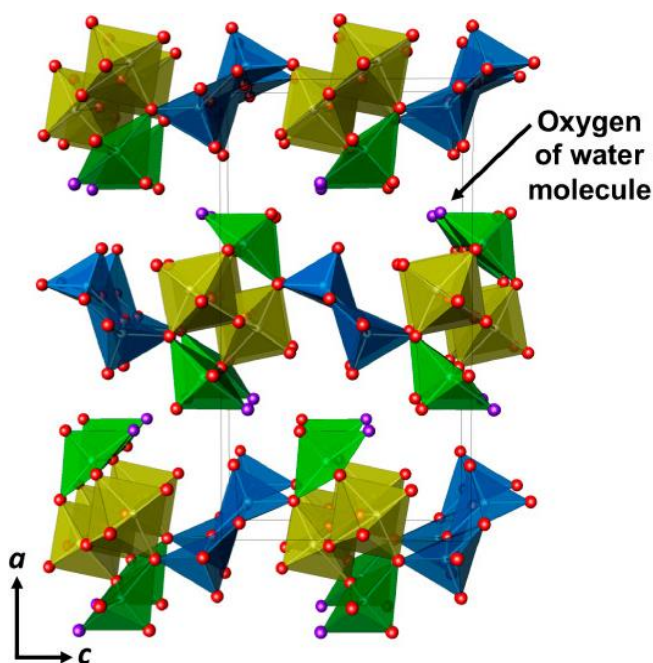


Figure 25 : Schematic illustration of the crystal structure of  $H_2V_3O_8$  with  $VO_6$  octahedra (yellow) and  $VO_5$  (green) and  $VO_5$  (blue) square pyramids. Hydrogen atoms are bonded to the oxygen atoms (purple), which are not shown<sup>50</sup>

$H_2V_3O_8$  adopts a hydrated layered structure<sup>50</sup>, comprised of  $V_3O_8$  layers linked by hydrogen bonds with each layer consisting of  $VO_6$  octahedra and  $VO_5$  trigonal bipyramids (fig 25). V exists in a mixed valence  $V^{5+}/V^{4+}$  state, leading to higher electrical conductivity compared to other Vanadium-based cathodes.

The discharge capacity of the initial cycle is found to be higher than the subsequent charge capacity by He et al<sup>50</sup>. Su et al<sup>61</sup> attribute this to the intercalation of  $Zn^{2+}$  in “dead sites”, that are electrochemically unfavourable to Zn extraction. Nonetheless, the cathode shows remarkable rate and cycling capability.

### 3.1.4 Other Vanadium Oxides

Lai et al<sup>51</sup> found significant difference in cycling performance between water intercalated  $V_6O_{13}$  and bare  $V_6O_{13}$ . The crystal structure of  $V_6O_{13}$  is composed of double layers of corner and edge sharing distorted  $VO_6$  octahedra. The intercalated water significantly increases interlamellar spacing and prevents irreversible Zn-insertion into “dead sites”, prolonging cycling life (fig 26).

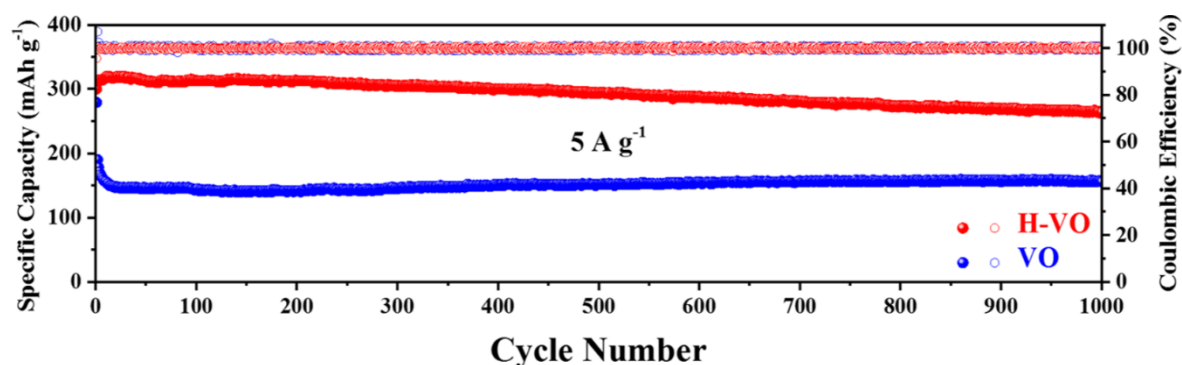


Figure 26 : Cycling performance of (H-VO)  $V_6O_{13} \cdot nH_2O$  and bare  $V_6O_{13}$  in 3M  $Zn(CF_3SO_3)_2$  aqueous electrolyte<sup>51</sup>



Wei et al<sup>52</sup> show a reversible transition to  $\text{Zn}_x\text{V}_{10}\text{O}_{24}\cdot n\text{H}_2\text{O}$  from bi-layered  $\text{V}_{10}\text{O}_{24}$  upon discharge. A large interlayer spacing of 14Å promotes a shorter diffusion pathway and allows intercalation of large hydrated ions with mixed valence states enhancing electroconductivity. The lack of long-range order also prevents stress from continual (de)intercalation of large cations.

### 3.2 Vanadates

Vanadates arise from the pre-intercalation of small and lightweight metal ions into existing vanadium oxide structures, allowing for increased structural stability and ultra-long cycling life with high rate capability.

Cathode	Electrolyte	Discharge Capacity (mAhg <sup>-1</sup> ) / Current Density (mA g <sup>-1</sup> )	Capacity Retention/ Charge Cycles/ Current Density (mA g <sup>-1</sup> )	Ref.
<b>Li<sub>x</sub>V<sub>2</sub>O<sub>5</sub>·nH<sub>2</sub>O</b>	2M ZnSO <sub>4</sub>	407.6/1000	~100%/800/10000	62
<b>Ag<sub>0.33</sub>V<sub>2</sub>O<sub>5</sub></b>	2M Zn(CF <sub>3</sub> SO <sub>3</sub> ) <sub>2</sub>	340/100	60%/500/100	63
<b>LiV<sub>3</sub>O<sub>8</sub></b>	1 M ZnSO <sub>4</sub>	172/133	75%/65/133	64
<b>Na<sub>0.33</sub>V<sub>2</sub>O<sub>5</sub></b>	3M Zn(CH <sub>3</sub> F <sub>3</sub> SO <sub>3</sub> ) <sub>2</sub>	367.1/100	93%/1000/1000	65
<b>NH<sub>4</sub>V<sub>4</sub>O<sub>10</sub></b>	3 M Zn(CF <sub>3</sub> SO <sub>3</sub> ) <sub>2</sub>	147/200	70%/5000/2000	66
<b>(NH<sub>4</sub>)<sub>2</sub>V<sub>10</sub>O<sub>25</sub>·8H<sub>2</sub>O</b>	3M Zn(CF <sub>3</sub> SO <sub>3</sub> ) <sub>2</sub> for capacity 2 M ZnSO <sub>4</sub> for cycling performance	288.8/100	90%/5000/5000	67
<b>Mg<sub>0.34</sub>V<sub>2</sub>O<sub>5</sub>·0.84H<sub>2</sub>O</b>	3 M Zn(CF <sub>3</sub> SO <sub>3</sub> ) <sub>2</sub>	353/100 and 264/1000	97%/2000/5000	68
<b>Na<sub>2</sub>V<sub>6</sub>O<sub>16</sub>·1.63H<sub>2</sub>O</b>	3M Zn(CF <sub>3</sub> SO <sub>3</sub> ) <sub>2</sub>	352/50 162/2000	90%/6000/5000	69
<b>Zn<sub>0.25</sub>V<sub>2</sub>O<sub>5</sub>·nH<sub>2</sub>O</b>	1M ZnSO <sub>4</sub>	282/300	~80%/1000/2400	70
<b>α-Zn<sub>2</sub>V<sub>2</sub>O<sub>7</sub></b>	1M ZnSO <sub>4</sub>	203.4/300	85%/1000/4000	71
<b>Na<sub>0.76</sub>V<sub>6</sub>O<sub>15</sub></b>	1M ZnSO <sub>4</sub>	135/500	90%/1000/2000	72
<b>HNaV<sub>6</sub>O<sub>16</sub>·4H<sub>2</sub>O</b>	1M ZnSO <sub>4</sub>	295.4/500	42%/2000/5000	72
<b>Na<sub>5</sub>V<sub>12</sub>O<sub>32</sub></b>	1M ZnSO <sub>4</sub>	244.5/500	71%/2000/4000	72
<b>NaV<sub>3</sub>O<sub>8</sub>·1.5H<sub>2</sub>O</b>	1M ZnSO <sub>4</sub> + 1M Na <sub>2</sub> SO <sub>4</sub>	380/50	82%/1000/4000	73
<b>Ca<sub>0.25</sub>V<sub>2</sub>O<sub>5</sub>·nH<sub>2</sub>O</b>	1M ZnSO <sub>4</sub>	340/50	96%/3000/20000	74
<b>K<sub>2</sub>V<sub>6</sub>O<sub>16</sub>·2.7H<sub>2</sub>O</b>	1M ZnSO <sub>4</sub>	320/200	82%/500/60000	75
<b>Fe<sub>5</sub>V<sub>15</sub>O<sub>39</sub>(OH)<sub>9</sub>·9H<sub>2</sub>O</b>	1M Zn(TFSI) <sub>2</sub>	385/100	80%/300/5000	76
<b>Zn<sub>3</sub>V<sub>2</sub>O<sub>7</sub>(OH)<sub>2</sub>·2H<sub>2</sub>O</b>	1M ZnSO <sub>4</sub>	213/50	68%/300/200	54

<b>NH<sub>4</sub>V<sub>4</sub>O<sub>10</sub></b>	2M ZnSO <sub>4</sub>	361.6/1000	90%/1000/10000	77
<b>Na<sub>2</sub>V<sub>6</sub>O<sub>16</sub>·3H<sub>2</sub>O</b>	1M ZnSO <sub>4</sub>	279.2/722	80%/1000/14440	78
<b>Zn<sub>x</sub>V<sub>2</sub>O<sub>5</sub>·nH<sub>2</sub>O</b>	3M Zn(CF <sub>3</sub> SO <sub>3</sub> ) <sub>2</sub>	470/200	91.1%/4000/5000	44

Table 3 : Electrochemical performance of vanadates in recent research in AZIBs

The majority of vanadates are tunnelled V<sub>2</sub>O<sub>5</sub> or layered V<sub>3</sub>O<sub>8</sub> structures (figs 27 & 28).

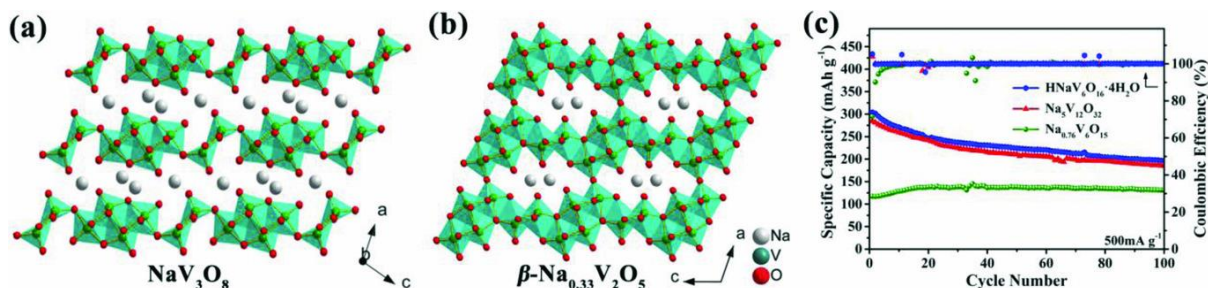


Figure 27 : Schematic illustration of the structure of pristine (a) layered NaV<sub>3</sub>O<sub>8</sub> and (b) tunnelled NaV<sub>2</sub>O<sub>5</sub> and associated short-term cycling performance<sup>72</sup> at 500mA g<sup>-1</sup> in 1M ZnSO<sub>4</sub>. Guo et al<sup>72</sup> tested the electrochemical properties of tunnelled Na<sub>0.76</sub>V<sub>6</sub>O<sub>15</sub>, with Na<sup>+</sup> in octahedral holes, and layered HNaV<sub>6</sub>O<sub>16</sub>·4H<sub>2</sub>O and Na<sub>5</sub>V<sub>12</sub>O<sub>32</sub>, where Na<sup>+</sup> occupy the interstitial tunnels.

The layered HNaV<sub>6</sub>O<sub>16</sub>·4H<sub>2</sub>O and Na<sub>5</sub>V<sub>12</sub>O<sub>32</sub> electrodes show similar cycling performance and intercalation mechanisms (figs 27c & 28). The cycling ability of the tunnelled Na<sub>0.76</sub>V<sub>6</sub>O<sub>15</sub> is better than the layered structures, indicating better structural stability where no irreversible phase transformation occurs during initial cycles.

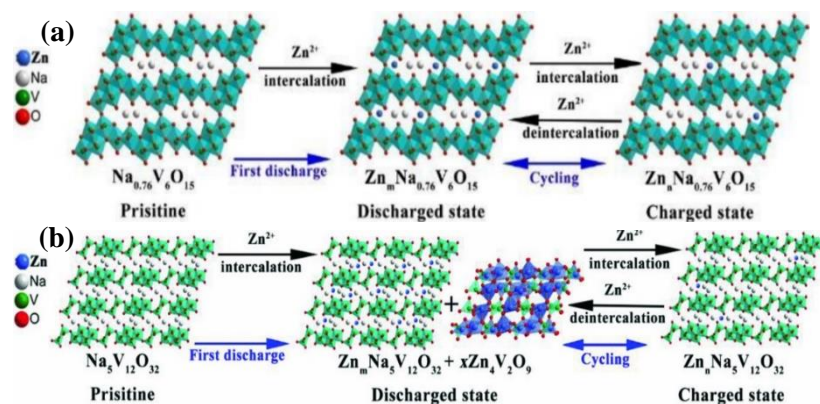


Figure 28 : Schematic illustration of the phase change upon cycling in (a) tunnelled Na<sub>0.76</sub>V<sub>6</sub>O<sub>15</sub> and (b) layered Na<sub>5</sub>V<sub>12</sub>O<sub>32</sub> in 1M ZnSO<sub>4</sub> electrolyte<sup>72</sup>

The initial discharge capacities of the layered structures are higher, indicating higher rate capabilities owing to the higher lattice spacing providing better diffusion pathways; however, reversible formation of a Zn<sub>4</sub>V<sub>2</sub>O<sub>9</sub> phase upon discharge leads to low capacity retention over cycling. Comparatively, the tunnel structure shows no morphological change upon cycling.

The proposed mechanism of the phase change in layered  $\text{HNaV}_6\text{O}_{16} \cdot 4\text{H}_2\text{O}$  and  $\text{Na}_5\text{V}_{12}\text{O}_{32}$  is as such:  $\text{Zn}^{2+}$  replaces the  $\text{Na}^+$  ion in the structure, due to its lower electrochemical potential, bonding with the unstable  $\text{V}_3\text{O}_8$  polyhedra via strong electrostatic interactions and decreasing the interlayer spacing, forming a  $\text{Zn}_4\text{V}_2\text{O}_9$  phase and releasing  $\text{Na}^+$  into the electrolyte. Addition of  $\text{Na}_2\text{SO}_4$  into the electrolyte is found to prevent this dissolution and improve short-term capacity retention by Guo et al<sup>72</sup> (figs 29 & 30).

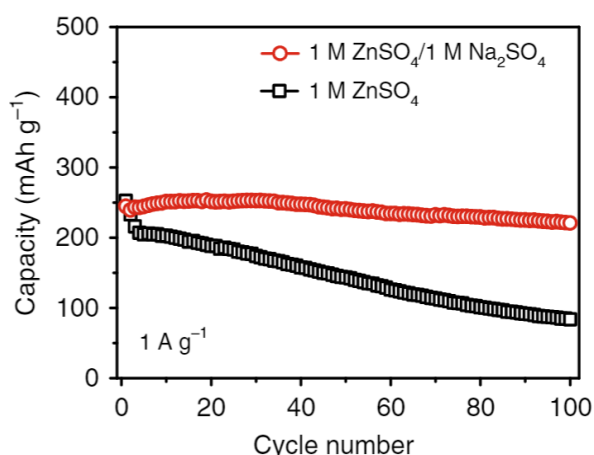


Figure 29 : Cycling performance of  $\text{Na}_{0.76}\text{V}_6\text{O}_{15}$  at  $1\text{A g}^{-1}$  with and without  $\text{Na}^+$  addition in  $1\text{M ZnSO}_4$  electrolyte<sup>72</sup>

On the contrary, He et al<sup>65</sup> find no  $\text{Na}^+$  dissolution in the tunnelled  $\text{Na}_{0.33}\text{V}_2\text{O}_5$  polymorph. The structure is maintained with very little cracking after 2000 cycles whereas that of  $\text{V}_2\text{O}_5$  shows

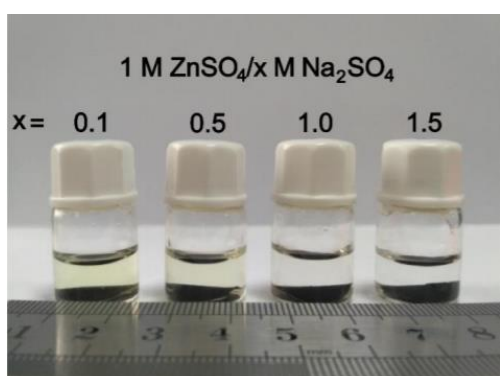


Figure 30 : Dissolution of the  $\text{Na}_{0.76}\text{V}_6\text{O}_{15}$  electrode dipped in  $\text{ZnSO}_4$  electrolyte<sup>72</sup>, showing a clearer solution (less dissolution) with increasing concentration (left to right) of pre-added  $\text{Na}^+$

great damage. This is attributed to increased stability provided by the  $\text{Na}^+$  acting as pillars in the electrode.

Wan et al<sup>73</sup> showed simultaneous reversible co-insertion of  $\text{Zn}^{2+}$  and  $\text{H}^+$  during discharge in  $\text{NaV}_3\text{O}_8 \cdot 1.5\text{H}_2\text{O}$ , forming  $\text{ZnSO}_4(\text{OH})_6 \cdot 4\text{H}_2\text{O}$  on the surface of the cathode, quite different to the  $\text{H}^+$ -conversion mechanism observed in  $\text{MnO}_2$ . Similar is reported by Sambandam et al<sup>71</sup> using layered  $\alpha\text{-Zn}_2\text{V}_2\text{O}_7$  as cathode. The structure consists of a tetrahedrally coordinated  $\text{VO}_4$  polyhedral layer lying between distorted trigonal bipyramid  $\text{ZnO}_5$  polyhedral layers and shows excellent cycling ability (fig 35). During discharge a new irreversible phase

$\text{Zn}_4(\text{OH})_6\text{SO}_4 \cdot 5\text{H}_2\text{O}$  is formed (fig 31) on the surface of the cathode<sup>54,63,78</sup>. Lee et al<sup>42</sup> denote this behaviour to the pH evolution of the electrolyte. Soundharrajan et al<sup>78</sup> showed that the higher the applied current, the more cycles were required to attain a stable discharge capacity in  $\text{Na}_2\text{V}_6\text{O}_{16} \cdot 3\text{H}_2\text{O}$  (fig 33).

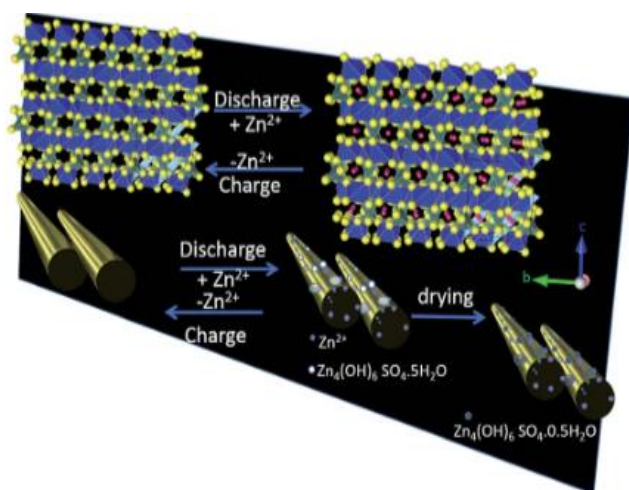


Figure 31 : Schematic illustration of the formation of  $\text{Zn}_4(\text{OH})_6\text{SO}_4 \cdot 5\text{H}_2\text{O}$  on cathode surface<sup>71</sup> in 1M  $\text{ZnSO}_4$

electrochemical properties in layered  $\text{LiV}_3\text{O}_8$ . Yang et al<sup>62</sup> report incomplete extraction of Zn ions. Lan et al<sup>63</sup> also show irreversible trapping of  $\text{Zn}^{2+}$  in “dead sites” in  $\text{Ag}_{0.33}\text{V}_2\text{O}_5$ . Upon discharge the silver is reduced and leached, while the  $\text{Zn}^{2+}$  occupies the empty sites leading to a new phase formation. This is a common problem in AZIBs.

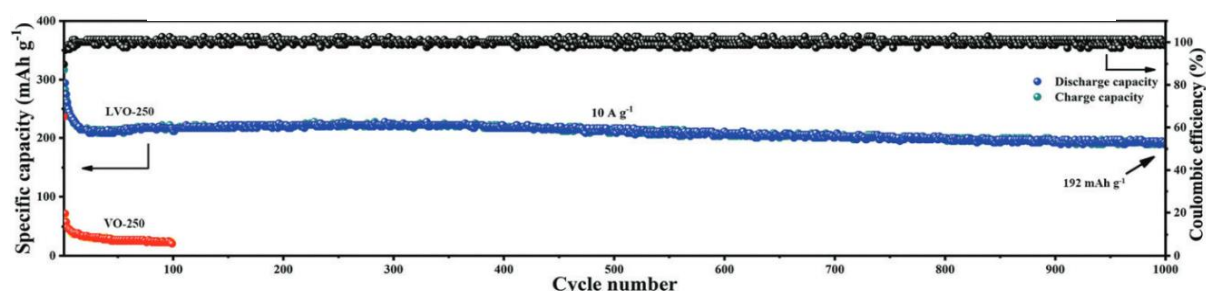


Figure 32 : Cycling performance of Lithium-intercalated  $\text{Li}_x\text{V}_2\text{O}_5 \cdot n\text{H}_2\text{O}$  (blue) and bare  $\text{V}_2\text{O}_5$  (red) at  $10\text{A g}^{-1}$  in 2M  $\text{ZnSO}_4$  aqueous electrolyte<sup>62</sup>

$\text{NH}_4$ -Vanadates have been extensively researched due to a lower molar mass than Na or K, theoretically resulting higher specific capacities, and a network of hydrogen bonds between the  $\text{NH}_4^+$  and vanadium oxides promoting structural stability. Tang et al<sup>77</sup> synthesized tunnelled  $\text{NH}_4\text{V}_4\text{O}_{10}$  and layered  $\text{NH}_4\text{V}_3\text{O}_8$  and  $(\text{NH}_4)_2\text{V}_3\text{O}_8$  (fig 37). The structure of  $\text{NH}_4\text{V}_4\text{O}_{10}$  is monoclinic with distorted edge-sharing  $\text{VO}_6$  octahedra forming a bilayered structure that comprises stacked  $\text{V}_4\text{O}_{10}$  units along the a-axis. The  $\text{NH}_4^+$  ions act as pillars between the layers.  $\text{NH}_4\text{V}_3\text{O}_8$  is composed of  $\text{VO}_5$  square pyramidal units and  $\text{VO}_6$  octahedra, while  $(\text{NH}_4)_2\text{V}_3\text{O}_8$  consists of corner-sharing  $\text{VO}_5$  square pyramids and  $\text{VO}_4$  tetrahedra.



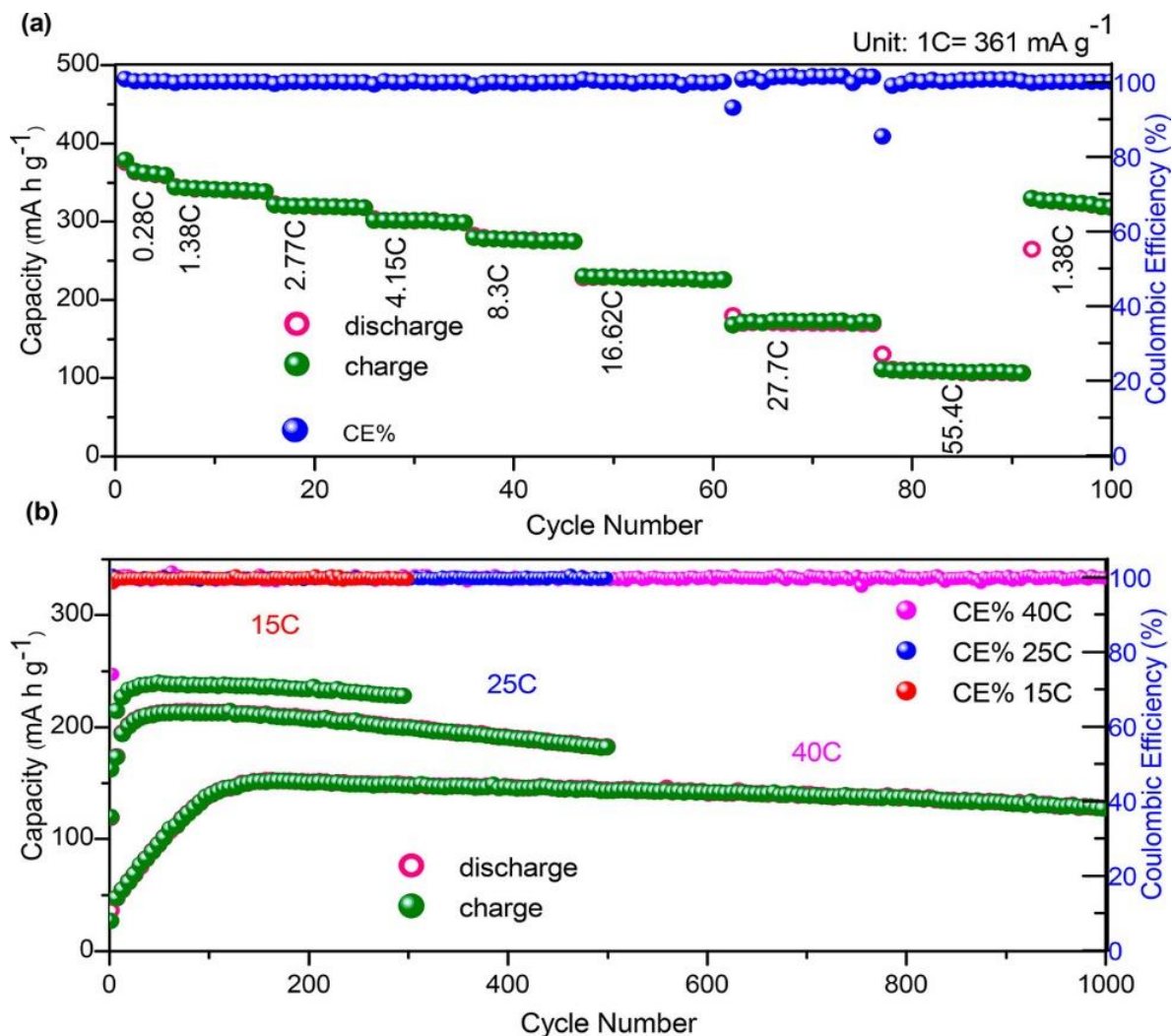


Figure 33 : Rate capabilities<sup>78</sup> of  $\text{Na}_2\text{V}_6\text{O}_{16} \cdot 3\text{H}_2\text{O}$  in 1M  $\text{ZnSO}_4$

$\text{NH}_4\text{V}_4\text{O}_{10}$  undergoes enlarged interlayer spacing to  $11.1\text{\AA}$  upon immersion in aqueous electrolytes (fig 39), owing to water-intercalation. Sambandam et al<sup>75</sup> show that water intercalation only occurs upon first discharge in  $\text{K}_2\text{V}_6\text{O}_{16}$ , leading to increasing discharge capacities in subsequent cycles (fig 36). Irreversible formation of Zn-intercalated  $\text{Zn}_3(\text{OH})_2\text{V}_2\text{O}_7 \cdot 2\text{H}_2\text{O}$  phase and partial Zn extraction is responsible for capacity fading in  $\text{NH}_4\text{V}_4\text{O}_{10}$ .

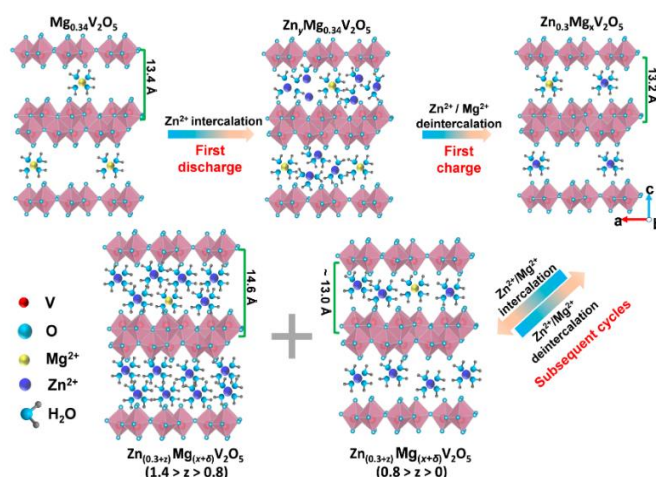


Figure 34 : Schematic illustration of the morphological evolution from  $\text{Mg}_{0.34}\text{V}_2\text{O}_5$  to  $\text{Zn}_y\text{Mg}_{0.34}\text{V}_2\text{O}_5$  upon first discharge<sup>68</sup> in 3 M  $\text{Zn}(\text{CF}_3\text{SO}_3)_2$



This limitation is not seen in layered  $(\text{NH}_4)_2\text{V}_3\text{O}_8$  or  $\text{NH}_4\text{V}_3\text{O}_8$ . Yang et al<sup>66</sup> show a change in morphology in nanobelt  $\text{NH}_4\text{V}_4\text{O}_{10}$  during charge storage. Upon discharge, the  $\text{NH}_4^+$  is irreversibly ejected into the electrolyte and leads to a transformation to bi-layered  $\text{Zn}_y\text{V}_4\text{O}_{10-x}\cdot\text{mH}_2\text{O}$ . Upon recharging, the extraction of  $\text{Zn}^{2+}$  produces electrostatic repulsion between the layers leading to formation of few-layer nanosheets. With re-injection of  $\text{Zn}^{2+}$ , the cations act as binders and stabilise the structure, re-establishing nanobelt morphology. Wei et al<sup>66</sup> use tunnelled  $(\text{NH}_4)_2\text{V}_{10}\text{O}_{25}\cdot 8\text{H}_2\text{O}$  and achieve even better results than Yang et al<sup>66</sup> with similar battery set ups.

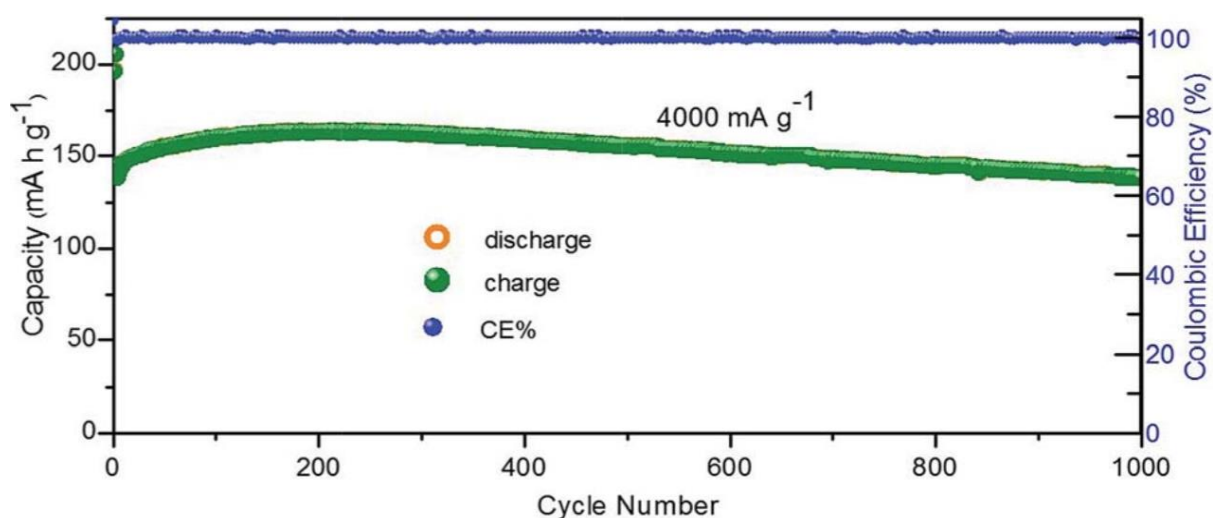


Figure 35 : Cycling performance of  $\alpha\text{-Zn}_2\text{V}_2\text{O}_7$  at  $4\text{Ag}^{-1}$  in 1M  $\text{ZnSO}_4$  aqueous electrolyte<sup>71</sup>

In 2018, Ming et al<sup>68</sup> reported using  $\text{Mg}^{2+}$  intercalated  $\text{Mg}_{0.34}\text{V}_2\text{O}_5\cdot 0.84\text{H}_2\text{O}$  nanobelts which allows for a larger interlayer spacing of  $13.4\text{\AA}$  compared to the commonly used  $\text{Li}^+$  intercalation. The  $\text{Mg}^{2+}$  is leaked out irreversibly into the electrolyte and replaced with  $\text{Zn}^{2+}$  ions (fig 34). Subsequent cycling follows from this new structure.

Xia et al<sup>74</sup> show an increase in interlayer spacing to 14.1 Å in  $\text{Ca}_{0.25}\text{V}_2\text{O}_5 \cdot n\text{H}_2\text{O}$ , a simple layered structure, like  $\text{ZnV}_2\text{O}_5$  with Cu ions resting in the interstitial spaces, when the electrode was immersed into the aqueous electrolyte. A similar, but smaller, increase is seen with  $\text{ZnV}_2\text{O}_5$ . The electrode is observed to slightly contract, rather than expand, upon Zn intercalation, attributed to the expulsion of water upon Zn intercalation, contrary to Tang et al's<sup>77</sup> findings.

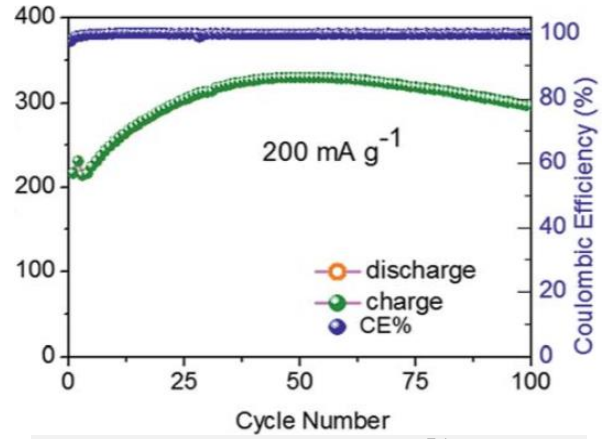


Figure 36 : Activation process<sup>75</sup> of layered  $\text{K}_2\text{V}_6\text{O}_{16}$  in 1M  $\text{ZnSO}_4$  from cycles 0 to 30 and subsequent capacity loss

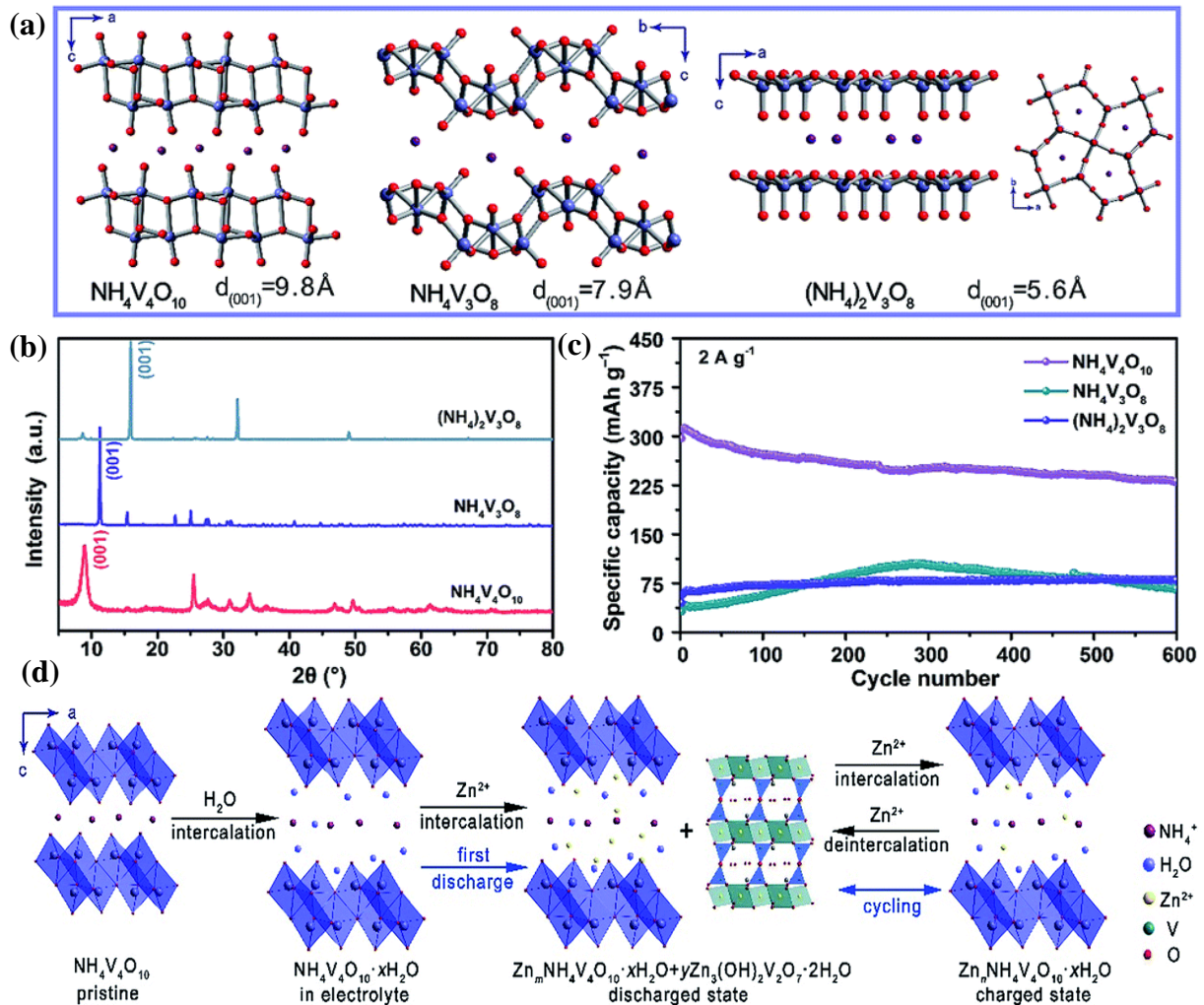


Figure 37 : (a) Schematic illustration of the structures of three different kinds of ammonium Vanadates and their interlayer spacing, (b) XRD patterns and (c) cycling performance at  $2 \text{ A g}^{-1}$  in aqueous electrolyte for each, and (d) phase evolution of  $\text{NH}_4\text{V}_4\text{O}_{10}$  upon immersion into aqueous electrolyte and subsequent discharge/ charge cycles<sup>77</sup>

### 3.3 Vanadium Phosphates

Vanadium phosphates typically exist in the NASICON structure, which is comprised of linked  $\text{ZrO}_6$  octahedra and  $\text{PO}_4/\text{SiO}_4$  tetrahedra that share common corners, forming interstitial channels.

Cathode	Electrolyte	Discharge Capacity ( $\text{mAhg}^{-1}$ ) / Current Density ( $\text{mA}\text{g}^{-1}$ )	Capacity Retention/ Charge Cycles/ Current Density ( $\text{mA}\text{g}^{-1}$ )	Ref.
$\text{Na}_3\text{V}_2(\text{PO}_4)_3/\text{C}$	0.5M $\text{Zn}(\text{CH}_3\text{COO})_2$	97/50	74%/100/50	38
$\text{Na}_3\text{V}_2(\text{PO}_4)_2\text{F}_3/\text{C}$	2M $\text{Zn}(\text{CF}_3\text{SO}_3)_2$	64.7/1000	95%/4000/1000	79
$\text{Na}_3\text{V}_2(\text{PO}_4)_3@\text{rGO}$	2M $\text{Zn}(\text{CF}_3\text{SO}_3)_2$	114/50 and 82/2000	75%/200/500	80
$\text{Na}_3\text{V}_2(\text{PO}_4)_3/\text{rGO}$	0.5M $\text{CH}_3\text{COONa}$ + 0.5M $\text{Zn}(\text{CH}_3\text{COO})_2$	60/2000	77%/200/50	81

Table 4 : Electrochemical performance of  $\text{MnO}_2$  based cathodes in recent research in AZIBs  
 Synthesis of electrodes on a pre-existing substrate, often with higher ionic conductivity, is commonly used to aid structural stability, contributing to greater cyclability. Li et al<sup>81</sup> synthesized (reduced graphene oxide) rGO (fig 38) and carbon backed  $\text{Na}_3\text{V}_2(\text{PO}_4)_3$  in a hybrid Na-Zn electrolyte where the  $\text{Na}^+$  acts as insertion ions on the cathode and  $\text{Zn}^{2+}$  ions contribute to stripping/plating on the anode. The Carbon and rGO improves the electroconductivity of the electrode, by forming a matrix that provides nucleation sites and a stable structure.

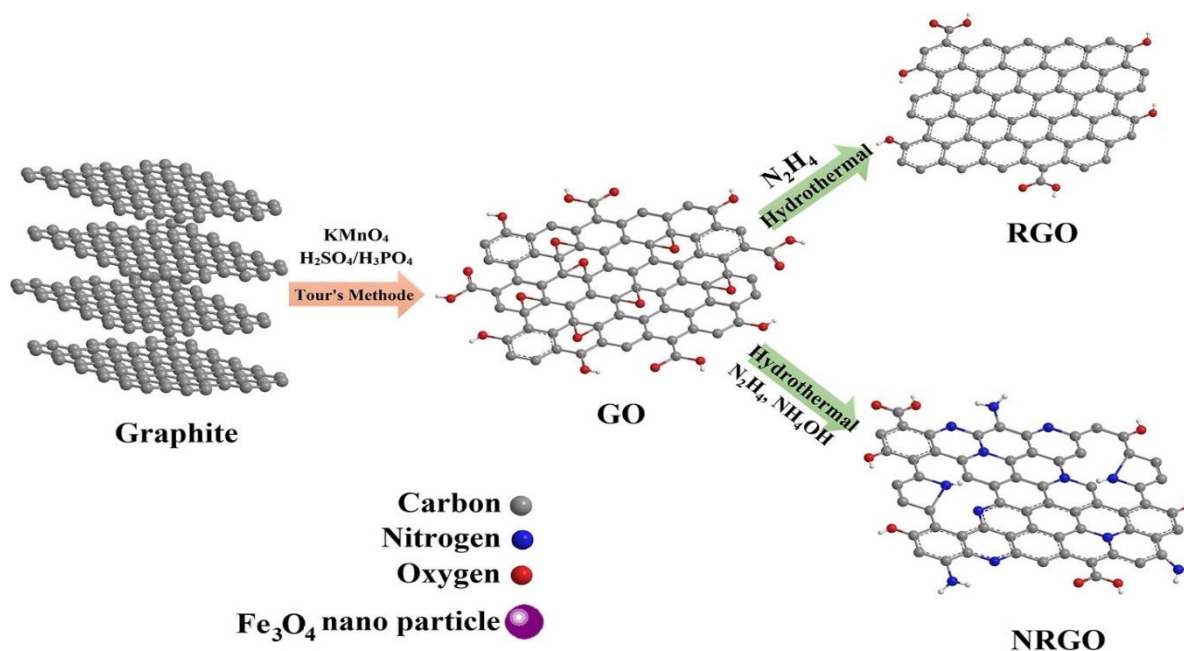


Figure 38 : Schematic illustration of the structure and synthesis of rGO from graphite<sup>81</sup>

Upon charging,  $\text{Na}^+$  are de-intercalated into the electrolyte with simultaneous Zn-ion plating on the Zn anode. After discharge, the cathode has undergone reversible morphological change to, with the reverse occurring upon discharge (fig 39). Li et al<sup>81</sup> note rapid capacity fading when  $\text{Na}_3\text{V}_2(\text{PO}_4)_3$  is used in acidic  $0.25\text{M Na}_2\text{SO}_4 + 0.5\text{M ZnSO}_4$  ( $\text{pH} \sim 4.45$ ) electrolyte compared to the mildly acidic ( $\text{pH} \sim 6.23$ ) electrolyte, purported to result from the dissolution of the cathode. In 2018, Li et al<sup>79</sup> reported formation of a solid electrolyte interphase (SEI) on  $\text{Na}_3\text{V}_2(\text{PO}_4)_2\text{F}_3$  cathode, commonly seen in Li-ion batteries, purported to be  $\text{ZnCO}_3$  and  $\text{ZnF}_2$  that is assumed to reduce the dissolution of the cathode in acidic  $2\text{M Zn}(\text{CF}_3\text{SO}_3)_2$  electrolyte.

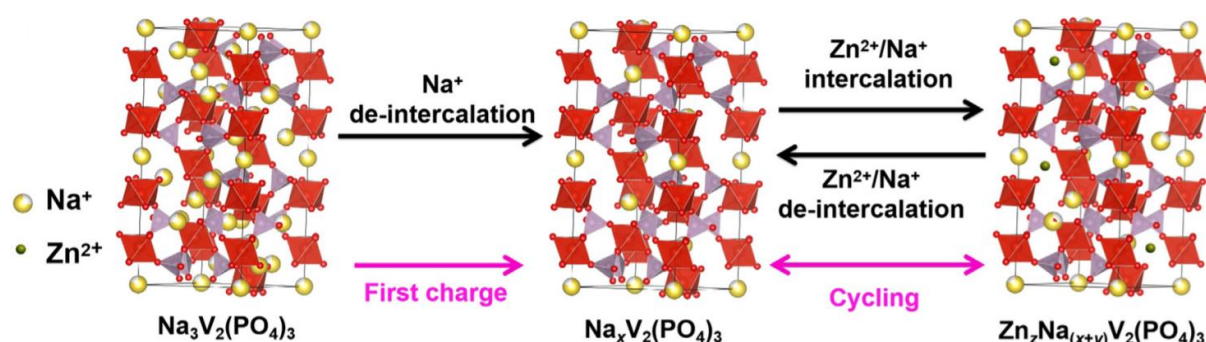


Figure 39 : Schematic illustration<sup>81</sup> of the phase change upon first and subsequent charge/discharge cycles in  $\text{Na}_3\text{V}_2(\text{PO}_4)_3$  in mildly acidic aqueous electrolyte

### 3.4 Sulphur-based Vanadium Compounds

Sulphur-based vanadium compounds typically show large rate capabilities due to their unique structure but suffer from poor cycling ability.

Cathode	Electrolyte	Discharge Capacity ( $\text{mAhg}^{-1}$ ) / Current Density ( $\text{mA}\text{g}^{-1}$ )	Capacity Retention/ Charge Cycles/ Current Density ( $\text{mA}\text{g}^{-1}$ )	Ref.
$\text{VS}_2$	$1\text{M ZnSO}_4$	190.3/50 and 115.5/2000	98%/200/500	83
$\text{VS}_4@\text{rGO}$	$1\text{M Zn}(\text{CF}_3\text{SO}_3)_2$	193/1000	93.3%/165/1000	84
$\text{VS}_4$	$1\text{M Zn}(\text{CF}_3\text{SO}_3)_2$	193/1000	93.3%/165/1000	84

Table 5 : Electrochemical performance of Sulphur-based Vanadium cathodes in recent research in AZIBs

$\text{VS}_2$  has a hexagonal layered structure with interlayer spacing of  $5.76\text{\AA}$ , formed of Vanadium layers in between Sulphur layers (fig 41). The cathode shows a simple intercalation mechanism with good electrochemical properties.



VS<sub>4</sub> has a peculiar crystallographic structure, built from V-S chains where each 1-dimensional chain is composed of a V<sup>4+</sup> and two S<sub>2</sub><sup>2-</sup> ions (fig 40a). The distance between two such chains is 6.2Å, larger than that of VS<sub>2</sub>, resulting in higher discharge capacities.

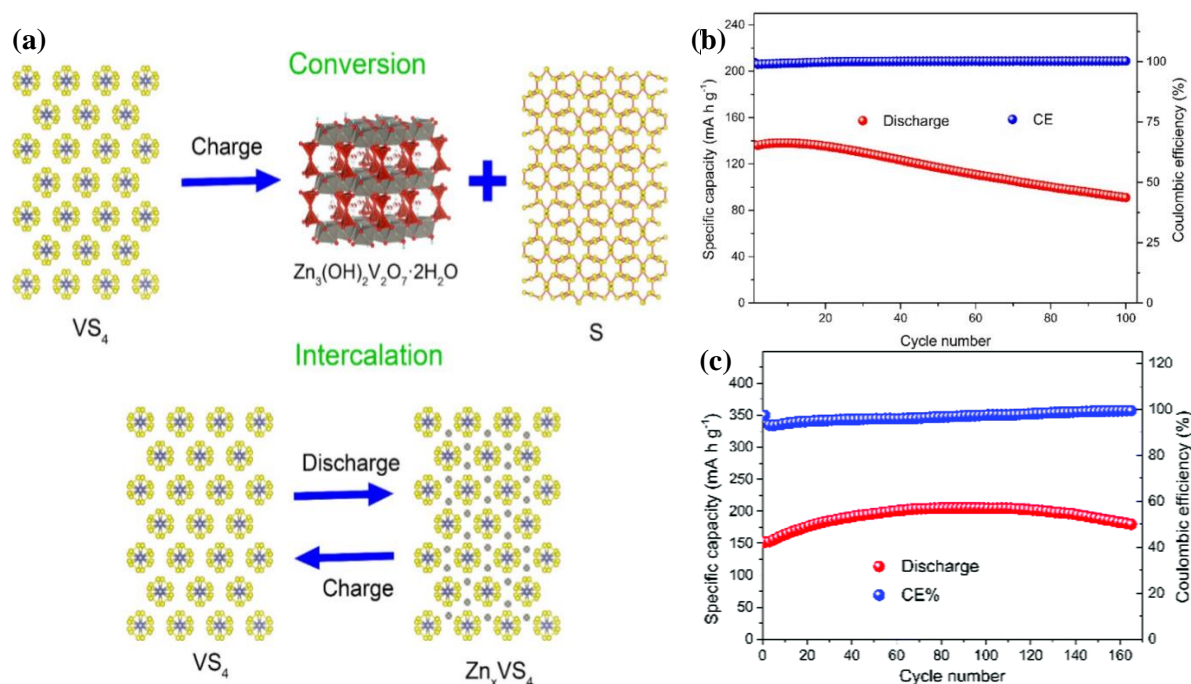


Figure 40 : (a) Schematic illustration of the conversion reaction mechanism in VS<sub>4</sub> upon cycling and cycling performance of (b) VS<sub>4</sub> and (c) VS<sub>4</sub>@rGO at 1Ag<sup>-1</sup> in 1M ZnSO<sub>4</sub> aqueous electrolyte<sup>84</sup>

In 2018, Qin et al<sup>84</sup> used rGO to provide structural support to the VS<sub>4</sub> framework, resulting in enhanced cycling ability (fig 40b, c). The cathode is reported to use simultaneous Zn-insertion and a conversion reaction for charge storage, where upon complete discharge, formation of Zn<sub>3</sub>(OH)<sub>2</sub>V<sub>2</sub>O<sub>7</sub>·2H<sub>2</sub>O is observed at 0.35V. This phase disappears and the original electrode is recovered when charged to 1.4V. Further charging to 1.8V results in the formation of Zn<sub>3</sub>(OH)<sub>2</sub>V<sub>2</sub>O<sub>7</sub>·2H<sub>2</sub>O again along with orthorhombic S<sub>8</sub> this time (fig 40a).

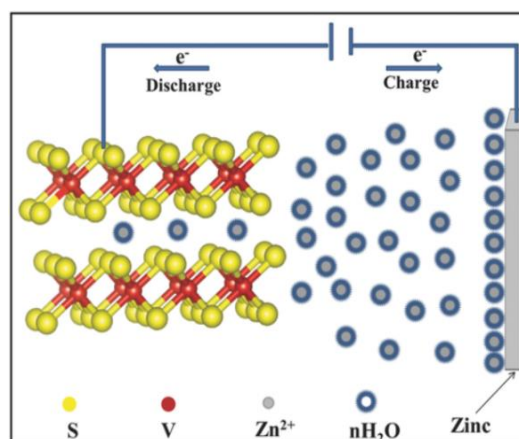


Figure 41 : Schematic illustration of the morphology of VS<sub>2</sub><sup>83</sup>



## 4 Prussian Blue Analogues

Prussian blue is a mixed valence<sup>89</sup>  $\text{Fe}^{2+}/\text{Fe}^{3+}$  inorganic complex with a dark blue colour. The generic Prussian blue analogue (PBA)<sup>90</sup> is  $\text{A}_x\text{M}_y[\text{M}_\text{B}(\text{CN})_6]_z \cdot n\text{H}_2\text{O}$  where  $\text{M}_\text{A}$  and  $\text{M}_\text{B}$  are usually Mn, Fe, Co, Ni, Cu and Zn and A is usually Li, Na or K. In battery chemistry, the typical PBA structure is a  $\text{MeFe}(\text{CN})_6$  (MeHCF) compound where the  $\text{Fe}(\text{CN})_6$  or hexacyanoferrate (HCF) (fig 42) provides a stable cubic open-framework structure allowing for easy intercalation of cations<sup>3,39</sup>.

Cathode	Electrolyte	Discharge Capacity (mAhg <sup>-1</sup> ) / Current Density (mA g <sup>-1</sup> )	Capacity Retention/ Charge Cycles/ Current (mA g <sup>-1</sup> )	Ref.
<b>CuHCF</b>	1M Na <sub>2</sub> SO <sub>4</sub> + 0.01M H <sub>2</sub> SO <sub>4</sub>	62/300	90%/300/300	85
<b>ZnHCF</b>	1M ZnSO <sub>4</sub>	65.4/60	81%/100/300	39
<b>Na<sub>2</sub>MnHCF</b>	1M Na <sub>2</sub> SO <sub>4</sub> + 1M ZnSO <sub>4</sub> + 0.0008M SDS	137/80	75%/2000/800	86
<b>NiHCF</b>	0.5M Na <sub>2</sub> SO <sub>4</sub> + 0.05M ZnSO <sub>4</sub>	76.2/100	81%/1000/100	3
<b>NaFe<sub>1.94</sub>(CN)<sub>6</sub></b>	1M Na <sub>2</sub> SO <sub>4</sub>	73.5/100	80%/1000/300	41
<b>ZnHCF@MnO<sub>2</sub></b>	0.5M ZnSO <sub>4</sub>	118/100	64%/1000/1000	40
<b>CuHCF</b>	1M ZnSO <sub>4</sub>	56/20	77%/20/20	87
<b>CuHCF</b>	0.02M ZnSO <sub>4</sub>	54/60	81%/100/600	88

Table 6 : Electrochemical performance of PBAs in recent research in AZIBs

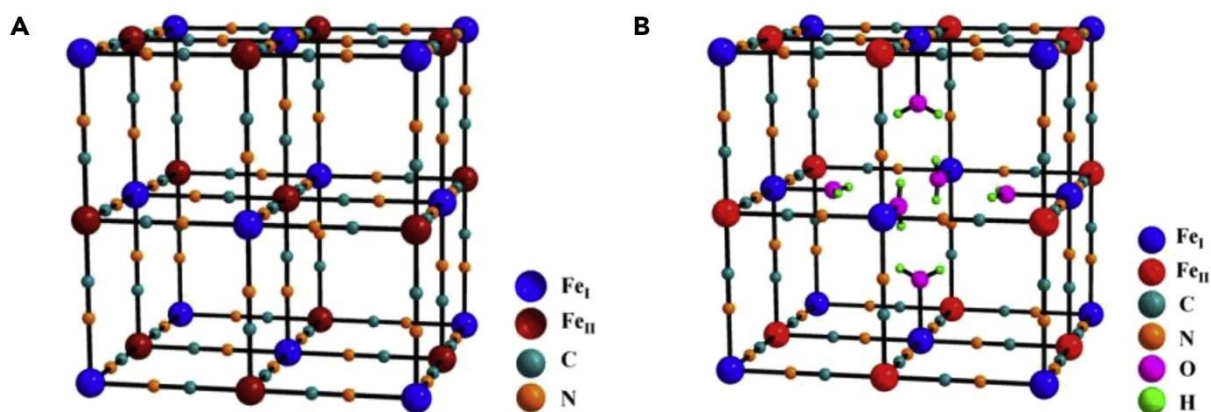


Figure 42 : Schematic illustration<sup>90</sup> of the structure of (A) anhydrous HCF and (B) hydrated HCF

The insertion<sup>87,88</sup> of  $\text{Zn}^{2+}$  results in the reduction of  $\text{Fe}^{3+}$  in the structure to  $\text{Fe}^{2+}$ . The use of PBAs in AZIBs normally results in  $\text{Zn}^{2+}$  poisoning at the cathode, resulting from irreversible Zn-ion insertion<sup>85,86</sup> (fig 43) and a gradual accumulation of Zinc in the framework. A large overpotential (fig 2) on charging, during which Zn plating occurs on the anode, results in  $\text{ZnO}$  and  $\text{Zn(OH)}_2$  dendrite formation, which is largely avoided by aqueous electrolytes otherwise, usually resulting in rapid capacity fading. To counter this, most approaches employ a dual-ion electrolyte.

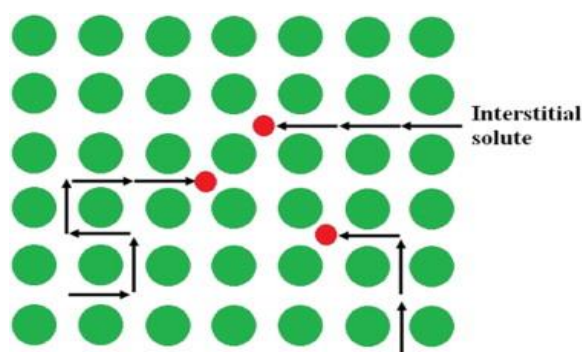


Figure 43 : Schematic illustration of direct interstitial insertion of  $\text{Zn}^{2+}$  in  $\text{CuHCF}$ <sup>86</sup>

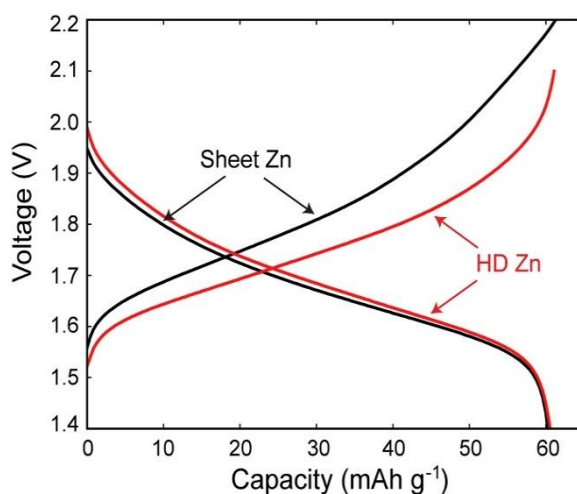


Figure 44 : Potential diagram of (hyper-dendritic) HD Zn showing a lower overpotential compared to sheet Zn on charging<sup>85</sup>

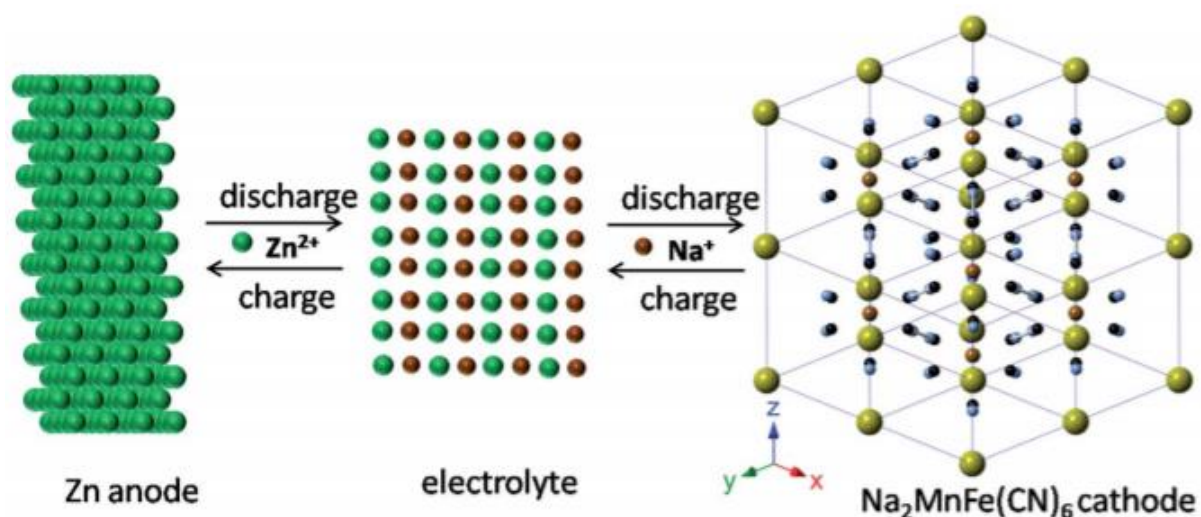


Figure 45 : Schematic illustration of the structure of Na<sub>2</sub>MnHCF cathode and charge/ discharge process in an aqueous hybrid Na-Zn electrolyte<sup>85</sup>

Gupta et al<sup>85</sup> use a dual-ion 100:1 Na<sub>2</sub>SO<sub>4</sub> to H<sub>2</sub>SO<sub>4</sub> electrolyte (fig 45), with Na<sup>+</sup> as the insertion/ extracted ion on the cathode and Zn<sup>2+</sup> stripping/ plating on the anode. The open cage-like structure of CuHCF allows for rapid (de)intercalation of cations without significant change to the crystal structure and the use of HD Zn as anode lowers the cathodic overpotential (fig 44) and allows for faster Zn plating/ stripping kinetics, preventing dendrite formation.

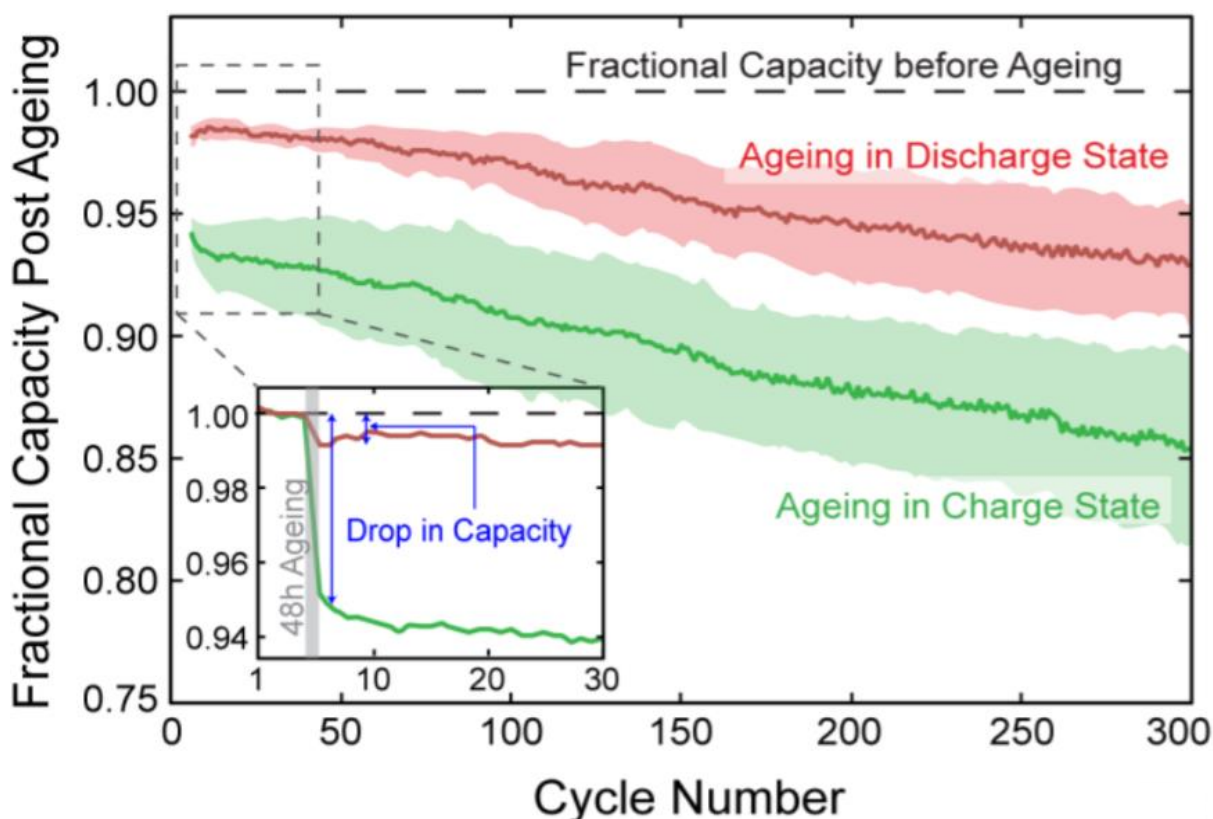


Figure 46 : Capacity fade due to Zn poisoning in CuHCF cathode after 48 hr rest<sup>85</sup> in 1M ZnSO<sub>4</sub> electrolyte. The capacity drop is greater when the battery is left in the charged state

Figure 46 demonstrates Zn-poisoning<sup>85</sup> where a fractional drop in capacity is seen after the battery was cycled at  $120\text{mA g}^{-1}$  for 4 cycles and then allowed to rest for 48 hours in the discharged and charged states. Capacity loss is greater when left in the charged state, when there is no  $\text{Na}^+$  presence in the PBA electrode, allowing easier irreversible intercalation of  $\text{Zn}^{2+}$  into the cathode, causing Zn-poisoning. In 2016, Kasiri et al<sup>91</sup> reported that a lower concentration of  $\text{Zn}^{2+}$  in the electrolyte

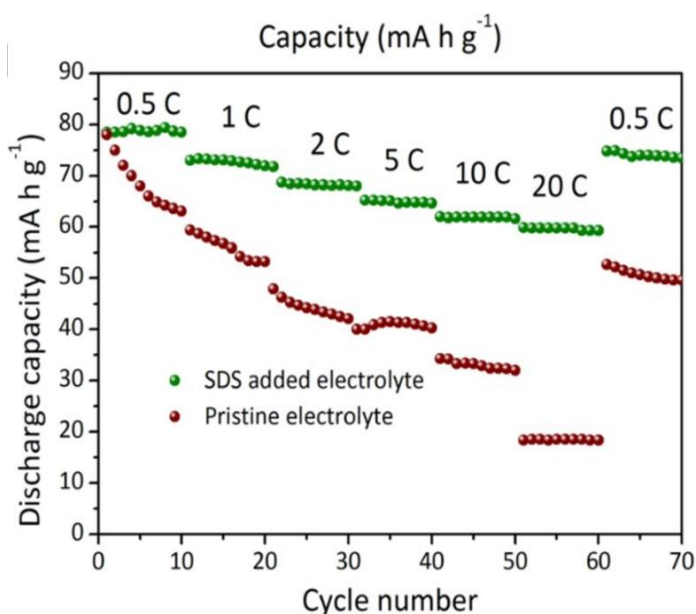


Figure 47 : Rate performance of  $\text{Na}_2\text{MnFe}(\text{CN})_6$  in pristine 1:1  $\text{Na}_2\text{SO}_4$  :  $\text{ZnSO}_4$  and  $0.8 \times 10^{-3}\text{M}$  SDS-added electrolyte<sup>86</sup>

promotes better cyclability of a CuHCF electrode.  $\text{Zn}^{2+}$  causes an irreversible phase transition in CuHCF where the cathode splits into CuHCF and atypical ZnHCF once a critical concentration of trapped  $\text{Zn}^{2+}$  is reached. This phase transition is found to occur over a greater number of cycles for lower current densities.

In 2017, Hou et al<sup>86</sup> showed that the addition of surfactant sodium dodecyl sulfate (SDS) in a hybrid Na-Zn electrolyte increased the operating voltage of AZIBs up to 2.5V by suppressing  $\text{H}_2/\text{O}_2$  evolution. The SDS molecules adsorb onto the electrode surface and suppress the evolution of hydrogen or oxygen upon cycling, preventing the decomposition of water and reducing electrode breakdown, thereby boosting rate performance (fig 47). It is proposed that the addition of surfactants in other AZIBs should provide similar benefits.

In 2017, Lu et al<sup>40</sup> showed that  $\text{MnO}_2$  birnessite nanosheet “wrapped” ZnHCF nanocubes giving ZnHCF@ $\text{MnO}_2$  results in improved cyclability in AZIBs. The ZnHCF acts as a  $\text{Zn}^{2+}$  reservoir while the  $\text{MnO}_2$  sheets provide structural stability.



## 5 Others

Various transition metal (TM) compounds and organics have also been explored and are summarised in table 7 for the interested reader.

Cathode	Electrolyte	Discharge Capacity (mAhg <sup>-1</sup> ) / Current Density (mA g <sup>-1</sup> )	Capacity Retention/ Charge Cycles/ Current Density (mA g <sup>-1</sup> )	Ref.
<b>Mo<sub>6</sub>S<sub>8</sub></b>	0.1M ZnSO <sub>4</sub>	57/128	61%/20/6.4	92
<b>LiMn<sub>0.8</sub>Fe<sub>0.2</sub>PO<sub>4</sub></b>	21M LiTGSi + 0.5M ZnSO <sub>4</sub>	110/137	~100%/150/51	58
<b>MnS</b>	2M ZnSO <sub>4</sub>	110/500	63.6%/100/500	8
<b>MoS<sub>2</sub></b>	2M ZnSO <sub>4</sub>	18/50	~100%/50/50	8
<b>WS<sub>2</sub></b>	2M ZnSO <sub>4</sub>	22/50	90%/50/50	8
<b>MoO<sub>3</sub></b>	2M ZnSO <sub>4</sub>	120/50	~1%/10/50	8
<b>Fe<sub>3</sub>O<sub>4</sub></b>	2M ZnSO <sub>4</sub>	45/100	33%/50/50	8
<b>TiO<sub>2</sub></b>	2M ZnSO <sub>4</sub>	4/50	50%/50/50	8
<b>TiB<sub>2</sub></b>	2M ZnSO <sub>4</sub>	~4/50	25%/50/50	8
<b>ZrB<sub>2</sub></b>	2M ZnSO <sub>4</sub>	~4/50	25%/50/50	8
<b>MoS<sub>2-x</sub></b>	3M Zn(OTf) <sub>2</sub>	100.9/1000	87.8/1000/1000	93
<b>Pyrene-4,5,9,10-tetrone (C<sub>16</sub>H<sub>6</sub>O<sub>4</sub>)</b>	2M ZnSO <sub>4</sub>	336/40 & 113/20000	67%/1000/3000	94
<b>Perylene-3,4,9,10-tetracarboxylic dianhydride/Ga (C<sub>24</sub>H<sub>8</sub>O<sub>6</sub>/Ga)</b>	2M ZnSO <sub>4</sub>	281/100	~100%/300/100	95
<b>Calix[4]quinone (C<sub>28</sub>H<sub>16</sub>O<sub>8</sub>)</b>	3M Zn(CF <sub>3</sub> SO <sub>3</sub> ) <sub>2</sub>	335/20	87%/1000/500	96
<b>Poly(aniline-co-azure B) (C<sub>6</sub>H<sub>5</sub>NH<sub>2</sub>-C<sub>15</sub>H<sub>16</sub>ClN<sub>3</sub>S)</b>	2M:3M ZnCl <sub>2</sub> :NH <sub>4</sub> Cl	127.8/1000	62%/180/200	97
<b>Poly(2,5-dihydroxy-1,4-benzoquinonyl sulphide)</b>	3M Zn(CF <sub>3</sub> SO <sub>3</sub> ) <sub>2</sub>	203/20	86%/50/40	98

Table 7 : Electrochemical performance of MnO<sub>2</sub> based cathodes in recent research in AZIBs

## 6 Summary and Further Outlook

Herein, we have summarised recent developments in manganese, vanadium, PBA and some organic and TM materials as cathodes for use in AZIBs. It is noted that preparation methods are crucial for the commercial viability of cathodes but have not been explicitly covered in this review.

MnO<sub>2</sub>-based cathodes show decent discharge capacities but complex charge-storage mechanisms that are still being debated. Activation processes, particularly in MnO<sub>2</sub> and vanadium cathodes typically result in Zn-intercalated materials or layered phases, and cation-leaching, in MnO<sub>2</sub> or sodium vanadates, leads to electrode destruction and low capacity retention. The use of SSWM, graphene, rGO or PANI along with addition of Mn<sup>2+</sup> and Na<sup>+</sup> in the electrolyte or use of CF<sub>3</sub>SO<sub>3</sub><sup>-</sup> anion have largely alleviated these issues. However, commercial synthesis of materials like rGO uses precursors that are toxic and difficult to work with<sup>99</sup> and lead to lower battery energy densities, negating the advantage of working with aqueous electrolytes.

PBAs appear unsuitable as cathode materials for conventional AZIBs due to zinc poisoning. While reducing Zn concentration in the electrolyte or wrapping the cathode in a separator that prevents Zn-intercalation have been found to alleviate poisoning<sup>85</sup>, PBA discharge capacities remain low. Similarly, vanadium phosphates show good cycling ability when co-synthesized with various frameworks but have generally low discharge capacities.

Sulphur-based vanadium compounds show good rate performance with further research needed to elucidate the long-term cycling characteristics.

Vanadates show impressive discharge capacities, cycling ability and rate performance. Organic materials provide a large, adaptable series of materials that can be fine-tuned, made environment friendly and we have an extensive knowledge in the commercial production of. Further research here could potentially lead to better batteries.

Avenues for further research include alleviating irreversible Zn-insertion in “dead sites”, possibly via pre-intercalation of small cations. While a critical problem in PBAs, this has been found to be a common issue in MnO<sub>2</sub> and vanadium cathodes. The use of surfactants could allow a large selection of cathodes to deliver larger voltages without H<sub>2</sub>/O<sub>2</sub> evolution, by reducing the contact area between water and the electrode. The use of various frameworks provides additional structural support, nucleation sites, increased surface area and higher

electroconductivities facilitating ion diffusion. Nano-structuring increases surface area and facilitates ion diffusion, leading to higher discharge and rate performances than bulk material electrodes. Defect engineering<sup>29,93</sup> is also a viable route to increasing performance, e.g. in  $\text{MoS}_{2-x}$  and  $\text{ZnMn}_{1.86}\text{Y}_{0.14}\text{O}_4$ .

This review hopes to have provided a timely and concise but extensive account of recent progress in the field of cathodes in AZIBs.

## 7 Bibliography

- 1 G. Ren, G. Ma and N. Cong, *Renewable and Sustainable Energy Reviews*, 2015, **41**, 225–236.
- 2 H. Chen, T. N. Cong, W. Yang, C. Tan, Y. Li and Y. Ding, *Progress in Natural Science*, 2009, **19**, 291–312.
- 3 K. Lu, B. Song, J. Zhang and H. Ma, A rechargeable Na-Zn hybrid aqueous battery fabricated with nickel hexacyanoferrate and nanostructured zinc, *Journal of Power Sources*, 2016, **321**, 257–263.
- 4 J. K. Seo, J. Shin, H. Chung, P. Y. Meng, X. Wang and Y. S. Meng, Intercalation and conversion reactions of nanosized  $\beta$ - $\text{MnO}_2$  cathode in the secondary Zn/ $\text{MnO}_2$  alkaline battery, *Journal of Physical Chemistry C*, 2018, **122**, 11177–11185.
- 5 B. J. Hertzberg, A. Huang, A. Hsieh, M. Chamoun, G. Davies, J. K. Seo, Z. Zhong, M. Croft, C. Erdonmez, Y. S. Meng and D. Steingart, Effect of Multiple Cation Electrolyte Mixtures on Rechargeable Zn- $\text{MnO}_2$  Alkaline Battery, *Chemistry of Materials*, 2016, **28**, 4536–4545.
- 6 H. Glatz, E. Tervoort and D. Kundu, Unveiling Critical Insight into the Zn Metal Anode Cyclability in Mildly Acidic Aqueous Electrolytes: Implications for Aqueous Zinc Batteries., *ACS applied materials & interfaces*, 2020, **12**, 3522–3530.
- 7 W. Tang, Y. Hou, F. Wang, L. Liu, Y. Wu and K. Zhu,  $\text{LiMn}_2\text{O}_4$  nanotube as cathode material of second-level charge capability for aqueous rechargeable batteries, *Nano Letters*, 2013, **13**, 2036–2040.
- 8 W. Liu, J. Hao, C. Xu, J. Mou, L. Dong, F. Jiang, Z. Kang, J. Wu, B. Jiang and F. Kang, Investigation of zinc ion storage of transition metal oxides, sulfides, and borides in zinc ion battery systems, *Chemical Communications*, 2017, **53**, 6872–6874.

- 9 H. Pan, Y. S. Hu and L. Chen, *Energy and Environmental Science*, 2013, 6, 2338–2360.
- 10 B. Scrosati and J. Garche, *Journal of Power Sources*, 2010, 195, 2419–2430.
- 11 N. Nitta, F. Wu, J. T. Lee and G. Yushin, *Materials Today*, 2015, 18, 252–264.
- 12 J. Hao, J. Long, B. Li, X. Li, S. Zhang, F. Yang, X. Zeng, Z. Yang, W. K. Pang and Z. Guo, Toward High-Performance Hybrid Zn-Based Batteries via Deeply Understanding Their Mechanism and Using Electrolyte Additive, *Advanced Functional Materials*, 2019, **29**, 1903605.
- 13 A. Naveed, H. Yang, J. Yang, Y. Nuli and J. Wang, Highly Reversible and Rechargeable Safe Zn Batteries Based on a Triethyl Phosphate Electrolyte, *Angewandte Chemie International Edition*, 2019, **58**, 2760–2764.
- 14 J. Wang, Y. Yamada, K. Sodeyama, E. Watanabe, K. Takada, Y. Tateyama and A. Yamada, Fire-extinguishing organic electrolytes for safe batteries, *Nature Energy*, 2018, **3**, 22–29.
- 15 B. Lee, H. R. Lee, H. Kim, K. Y. Chung, B. W. Cho and S. H. Oh, Elucidating the intercalation mechanism of zinc ions into  $\alpha$ -MnO<sub>2</sub> for rechargeable zinc batteries, *Chemical Communications*, 2015, **51**, 9265–9268.
- 16 B. Lee, C. S. Yoon, H. R. Lee, K. Y. Chung, B. W. Cho and S. H. Oh, Electrochemically-induced reversible transition from the tunneled to layered polymorphs of manganese dioxide, *Scientific Reports*, 2014, **4**, 1–8.
- 17 H. Pan, Y. Shao, P. Yan, Y. Cheng, K. S. Han, Z. Nie, C. Wang, J. Yang, X. Li, P. Bhattacharya, K. T. Mueller and J. Liu, Reversible aqueous zinc/manganese oxide energy storage from conversion reactions, *Nature Energy*, 2016, **1**, 1–7.
- 18 S. Islam, M. H. Alfaruqi, V. Mathew, J. Song, S. Kim, S. Kim, J. Jo, J. P. Baboo, D. T. Pham, D. Y. Putro, Y. K. Sun and J. Kim, Facile synthesis and the exploration of the zinc storage mechanism of  $\beta$ -MnO<sub>2</sub> nanorods with exposed (101) planes as a novel cathode material for high performance eco-friendly zinc-ion batteries, *Journal of Materials Chemistry A*, 2017, **5**, 23299–23309.



- 19 N. Zhang, F. Cheng, J. Liu, L. Wang, X. Long, X. Liu, F. Li and J. Chen, Rechargeable aqueous zinc-manganese dioxide batteries with high energy and power densities, *Nature Communications*, 2017, **8**, 1–9.
- 20 M. H. Alfaruqi, S. Islam, D. Y. Putro, V. Mathew, S. Kim, J. Jo, S. Kim, Y. K. Sun, K. Kim and J. Kim, Structural transformation and electrochemical study of layered MnO<sub>2</sub> in rechargeable aqueous zinc-ion battery, *Electrochimica Acta*, 2018, **276**, 1–11.
- 21 M. H. Alfaruqi, J. Gim, S. Kim, J. Song, D. T. Pham, J. Jo, Z. Xiu, V. Mathew and J. Kim, A layered  $\delta$ -MnO<sub>2</sub> nanoflake cathode with high zinc-storage capacities for eco-friendly battery applications, *Electrochemistry Communications*, 2015, **60**, 121–125.
- 22 S. Komaba, N. Kumagai and S. Chiba, Synthesis of layered MnO<sub>2</sub> by calcination of KMnO<sub>4</sub> for rechargeable lithium battery cathode, *Electrochimica Acta*, 2000, **46**, 31–37.
- 23 S. Devaraj and N. Munichandraiah, Effect of crystallographic structure of MnO<sub>2</sub> on its electrochemical capacitance properties, *Journal of Physical Chemistry C*, 2008, **112**, 4406–4417.
- 24 C. Wang, Y. Zeng, X. Xiao, S. Wu, G. Zhong, K. Xu, Z. Wei, W. Su and X. Lu,  $\gamma$ -MnO<sub>2</sub> nanorods/graphene composite as efficient cathode for advanced rechargeable aqueous zinc-ion battery, *Journal of Energy Chemistry*, 2020, **43**, 182–187.
- 25 M. H. Alfaruqi, V. Mathew, J. Gim, S. Kim, J. Song, J. P. Baboo, S. H. Choi and J. Kim, Electrochemically induced structural transformation in a  $\gamma$ -MnO<sub>2</sub> cathode of a high capacity zinc-ion battery system, *Chemistry of Materials*, 2015, **27**, 3609–3620.
- 26 J. Hao, J. Mou, J. Zhang, L. Dong, W. Liu, C. Xu and F. Kang, Electrochemically induced spinel-layered phase transition of Mn<sub>3</sub>O<sub>4</sub> in high performance neutral aqueous rechargeable zinc battery, *Electrochimica Acta*, 2018, **259**, 170–178.
- 27 C. Zhu, G. Fang, J. Zhou, J. Guo, Z. Wang, C. Wang, J. Li, Y. Tang and S. Liang, Binder-free stainless steel@Mn<sub>3</sub>O<sub>4</sub> nanoflower composite: A high-activity aqueous zinc-ion battery cathode with high-capacity and long-cycle-life, *Journal of Materials Chemistry A*, 2018, **6**, 9677–9683.

- 28 J. Huang, Z. Wang, M. Hou, X. Dong, Y. Liu, Y. Wang and Y. Xia, Polyaniline-intercalated manganese dioxide nanolayers as a high-performance cathode material for an aqueous zinc-ion battery, *Nature Communications*, 2018, **9**, 1–8.
- 29 N. Zhang, F. Cheng, Y. Liu, Q. Zhao, K. Lei, C. Chen, X. Liu and J. Chen, Cation-Deficient Spinel  $\text{ZnMn}_2\text{O}_4$  Cathode in  $\text{Zn}(\text{CF}_3\text{SO}_3)_2$  Electrolyte for Rechargeable Aqueous Zn-Ion Battery, *Journal of the American Chemical Society*, 2016, **138**, 12894–12901.
- 30 X. Wu, Y. Xiang, Q. Peng, X. Wu, Y. Li, F. Tang, R. Song, Z. Liu, Z. He and X. Wu, Green-low-cost rechargeable aqueous zinc-ion batteries using hollow porous spinel  $\text{ZnMn}_2\text{O}_4$  as the cathode material, *Journal of Materials Chemistry A*, 2017, **5**, 17990–17997.
- 31 M. H. Alfaruqi, S. Islam, V. Mathew, J. Song, S. Kim, D. P. Tung, J. Jo, S. Kim, J. P. Baboo, Z. Xiu and J. Kim, Ambient redox synthesis of vanadium-doped manganese dioxide nanoparticles and their enhanced zinc storage properties, *Applied Surface Science*, 2017, **404**, 435–442.
- 32 Q. Feng, K. Yanagisawa and N. Yamasaki, *Hydrothermal Soft Chemical Process for Synthesis of Manganese Oxides with Tunnel Structures*, 1998, vol. 18.
- 33 J. Lee, J. B. Ju, W. il Cho, B. W. Cho and S. H. Oh, Todorokite-type  $\text{MnO}_2$  as a zinc-ion intercalating material, *Electrochimica Acta*, 2013, **112**, 138–143.
- 34 C. Xu, B. Li, H. Du and F. Kang, Energetic Zinc Ion Chemistry: The Rechargeable Zinc Ion Battery, *Angewandte Chemie International Edition*, 2012, **51**, 933–935.
- 35 F. Wang, X. Wang, Z. Chang, Y. Zhu, L. Fu, X. Liu and Y. Wu, *Nanoscale Horizons*, 2016, **1**, 272–289.
- 36 D. Su, H. J. Ahn and G. Wang,  $\beta$ - $\text{MnO}_2$  nanorods with exposed tunnel structures as high-performance cathode materials for sodium-ion batteries, *NPG Asia Materials*, 2013, **5**, e70–e70.
- 37 L. Wang, X. He, W. Sun, J. Wang, Y. Li and S. Fan, Crystal orientation tuning of  $\text{LiFePO}_4$  nanoplates for high rate lithium battery cathode materials, *Nano Letters*, 2012, **12**, 5632–5636.

- 38 G. Li, Z. Yang, Y. Jiang, C. Jin, W. Huang, X. Ding and Y. Huang, Towards polyvalent ion batteries: A zinc-ion battery based on NASICON structured  $\text{Na}_3\text{V}_2(\text{PO}_4)_3$ , *Nano Energy*, 2016, **25**, 211–217.
- 39 L. Zhang, L. Chen, X. Zhou and Z. Liu, Towards high-voltage aqueous metal-ion batteries beyond 1.5 V: The zinc/zinc hexacyanoferrate system, *Advanced Energy Materials*, 2015, **5**, 1400930.
- 40 K. Lu, B. Song, Y. Zhang, H. Ma and J. Zhang, Encapsulation of zinc hexacyanoferrate nanocubes with manganese oxide nanosheets for high-performance rechargeable zinc ion batteries, *Journal of Materials Chemistry A*, 2017, **5**, 23628–23633.
- 41 L. P. Wang, P. F. Wang, T. S. Wang, Y. X. Yin, Y. G. Guo and C. R. Wang, Prussian blue nanocubes as cathode materials for aqueous Na-Zn hybrid batteries, *Journal of Power Sources*, 2017, **355**, 18–22.
- 42 B. Lee, H. R. Seo, H. R. Lee, C. S. Yoon, J. H. Kim, K. Y. Chung, B. W. Cho and S. H. Oh, Critical Role of pH Evolution of Electrolyte in the Reaction Mechanism for Rechargeable Zinc Batteries, *ChemSusChem*, 2016, **9**, 2948–2956.
- 43 X. Chen, L. Wang, H. Li, F. Cheng and J. Chen, Porous  $\text{V}_2\text{O}_5$  nanofibers as cathode materials for rechargeable aqueous zinc-ion batteries, *Journal of Energy Chemistry*, 2019, **38**, 20–25.
- 44 N. Zhang, Y. Dong, M. Jia, X. Bian, Y. Wang, M. Qiu, J. Xu, Y. Liu, L. Jiao and F. Cheng, Rechargeable Aqueous Zn- $\text{V}_2\text{O}_5$  Battery with High Energy Density and Long Cycle Life, *ACS Energy Letters*, 2018, **3**, 1366–1372.
- 45 P. Hu, M. Yan, T. Zhu, X. Wang, X. Wei, J. Li, L. Zhou, Z. Li, L. Chen and L. Mai, Zn/ $\text{V}_2\text{O}_5$  Aqueous Hybrid-Ion Battery with High Voltage Platform and Long Cycle Life, *ACS Applied Materials and Interfaces*, 2017, **9**, 42717–42722.
- 46 L. Chen, Y. Ruan, G. Zhang, Q. Wei, Y. Jiang, T. Xiong, P. He, W. Yang, M. Yan, Q. An and L. Mai, Ultrastable and High-Performance Zn/ $\text{VO}_2$  Battery Based on a Reversible Single-Phase Reaction, *Chemistry of Materials*, 2019, **31**, 699–706.

- 47 J. Ding, Z. Du, L. Gu, B. Li, L. Wang, S. Wang, Y. Gong and S. Yang, Ultrafast Zn<sup>2+</sup> Intercalation and Deintercalation in Vanadium Dioxide, *Advanced Materials*, 2018, **30**, 1800762.
- 48 T. Wei, Q. Li, G. Yang and C. Wang, An electrochemically induced bilayered structure facilitates long-life zinc storage of vanadium dioxide, *Journal of Materials Chemistry A*, 2018, **6**, 8006–8012.
- 49 X. Dai, F. Wan, L. Zhang, H. Cao and Z. Niu, Freestanding graphene/VO<sub>2</sub> composite films for highly stable aqueous Zn-ion batteries with superior rate performance, *Energy Storage Materials*, 2019, **17**, 143–150.
- 50 P. He, Y. Quan, X. Xu, M. Yan, W. Yang, Q. An, L. He and L. Mai, High-Performance Aqueous Zinc–Ion Battery Based on Layered H<sub>2</sub>V<sub>3</sub>O<sub>8</sub> Nanowire Cathode, *Small*, 2017, **13**, 1702551.
- 51 J. Lai, H. Zhu, X. Zhu, H. Koritala and Y. Wang, Interlayer-Expanded V<sub>6</sub>O<sub>13</sub>·nH<sub>2</sub>O Architecture Constructed for an Advanced Rechargeable Aqueous Zinc-Ion Battery, *ACS Applied Energy Materials*, 2019, **2**, 1988–1996.
- 52 T. Wei, Q. Li, G. Yang and C. Wang, High-rate and durable aqueous zinc ion battery using dendritic V<sub>10</sub>O<sub>24</sub>·12H<sub>2</sub>O cathode material with large interlamellar spacing, *Electrochimica Acta*, 2018, **287**, 60–67.
- 53 M. Yan, P. He, Y. Chen, S. Wang, Q. Wei, K. Zhao, X. Xu, Q. An, Y. Shuang, Y. Shao, K. T. Mueller, L. Mai, J. Liu and J. Yang, Water-Lubricated Intercalation in V<sub>2</sub>O<sub>5</sub>·nH<sub>2</sub>O for High-Capacity and High-Rate Aqueous Rechargeable Zinc Batteries, *Advanced Materials*, 2018, **30**, 1703725.
- 54 C. Xia, J. Guo, Y. Lei, H. Liang, C. Zhao and H. N. Alshareef, Rechargeable Aqueous Zinc-Ion Battery Based on Porous Framework Zinc Pyrovanadate Intercalation Cathode, *Advanced Materials*, 2018, **30**, 1705580.
- 55 A. Gambou-Bosca and D. Bélanger, Electrochemical characterization of MnO<sub>2</sub>-based composite in the presence of salt-in-water and water-in-salt electrolytes as electrode for electrochemical capacitors, *Journal of Power Sources*, 2016, **326**, 595–603.



- 56 L. Suo, O. Borodin, T. Gao, M. Olguin, J. Ho, X. Fan, C. Luo, C. Wang and K. Xu, “Water-in-salt” electrolyte enables high-voltage aqueous lithium-ion chemistries, *Science*, 2015, **350**, 938–943.
- 57 L. Suo, O. Borodin, W. Sun, X. Fan, C. Yang, F. Wang, T. Gao, Z. Ma, M. Schroeder, A. von Cresce, S. M. Russell, M. Armand, A. Angell, K. Xu and C. Wang, Advanced High-Voltage Aqueous Lithium-Ion Battery Enabled by “Water-in-Bisalt” Electrolyte, *Angewandte Chemie - International Edition*, 2016, **55**, 7136–7141.
- 58 J. Zhao, Y. Li, X. Peng, S. Dong, J. Ma, G. Cui and L. Chen, High-voltage Zn/LiMn<sub>0.8</sub>Fe<sub>0.2</sub>PO<sub>4</sub> aqueous rechargeable battery by virtue of “water-in-salt” electrolyte, *Electrochemistry Communications*, 2016, **69**, 6–10.
- 59 S. Lee, I. N. Ivanov, J. K. Keum and H. Nyung Lee, *Epitaxial stabilization and phase instability of VO<sub>2</sub> polymorphs*, .
- 60 B. Tang, G. Fang, J. Zhou, L. Wang, Y. Lei, C. Wang, T. Lin, Y. Tang and S. Liang, Potassium vanadates with stable structure and fast ion diffusion channel as cathode for rechargeable aqueous zinc-ion batteries, *Nano Energy*, 2018, **51**, 579–587.
- 61 D. Su and G. Wang, Single-crystalline bilayered V<sub>2</sub>O<sub>5</sub> nanobelts for high-capacity sodium-ion batteries, *ACS Nano*, 2013, **7**, 11218–11226.
- 62 Y. Yang, Y. Tang, G. Fang, L. Shan, J. Guo, W. Zhang, C. Wang, L. Wang, J. Zhou and S. Liang, Li<sup>+</sup> intercalated V<sub>2</sub>O<sub>5</sub>·N H<sub>2</sub>O with enlarged layer spacing and fast ion diffusion as an aqueous zinc-ion battery cathode, *Energy and Environmental Science*, 2018, **11**, 3157–3162.
- 63 B. Lan, Z. Peng, L. Chen, C. Tang, S. Dong, C. Chen, M. Zhou, C. Chen, Q. An and P. Luo, Metallic silver doped vanadium pentoxide cathode for aqueous rechargeable zinc ion batteries, *Journal of Alloys and Compounds*, 2019, **787**, 9–16.
- 64 M. H. Alfaruqi, V. Mathew, J. Song, S. Kim, S. Islam, D. T. Pham, J. Jo, S. Kim, J. P. Baboo, Z. Xiu, K. S. Lee, Y. K. Sun and J. Kim, Electrochemical Zinc Intercalation in Lithium Vanadium Oxide: A High-Capacity Zinc-Ion Battery Cathode, *Chemistry of Materials*, 2017, **29**, 1684–1694.

- 65 P. He, G. Zhang, X. Liao, M. Yan, X. Xu, Q. An, J. Liu and L. Mai, Sodium Ion Stabilized Vanadium Oxide Nanowire Cathode for High-Performance Zinc-Ion Batteries, *Advanced Energy Materials*, 2018, **8**, 1702463.
- 66 G. Yang, T. Wei and C. Wang, Self-Healing Lamellar Structure Boosts Highly Stable Zinc-Storage Property of Bilayered Vanadium Oxides, *ACS Applied Materials and Interfaces*, 2018, **10**, 35079–35089.
- 67 T. Wei, Q. Li, G. Yang and C. Wang, Highly reversible and long-life cycling aqueous zinc-ion battery based on ultrathin  $(\text{NH}_4)_2\text{V}_{10}\text{O}_{25} \cdot 8\text{H}_2\text{O}$  nanobelts, *Journal of Materials Chemistry A*, 2018, **6**, 20402–20410.
- 68 F. Ming, H. Liang, Y. Lei, S. Kandambeth, M. Eddaoudi and H. N. Alshareef, Layered  $\text{Mg}_x\text{V}_2\text{O}_5 \cdot n\text{H}_2\text{O}$  as Cathode Material for High-Performance Aqueous Zinc Ion Batteries, *ACS Energy Letters*, 2018, **3**, 2602–2609.
- 69 P. Hu, T. Zhu, X. Wang, X. Wei, M. Yan, J. Li, W. Luo, W. Yang, W. Zhang, L. Zhou, Z. Zhou and L. Mai, Highly Durable  $\text{Na}_2\text{V}_6\text{O}_{16} \cdot 1.63\text{H}_2\text{O}$  Nanowire Cathode for Aqueous Zinc-Ion Battery, *Nano Letters*, 2018, **18**, 1758–1763.
- 70 D. Kundu, B. D. Adams, V. Duffort, S. H. Vajargah and L. F. Nazar, A high-capacity and long-life aqueous rechargeable zinc battery using a metal oxide intercalation cathode, *Nature Energy*, 2016, **1**, 1–8.
- 71 B. Sambandam, V. Soundharrajan, S. Kim, M. H. Alfaruqi, J. Jo, S. Kim, V. Mathew, Y. K. Sun and J. Kim, Aqueous rechargeable Zn-ion batteries: An imperishable and high-energy  $\text{Zn}_2\text{V}_2\text{O}_7$  nanowire cathode through intercalation regulation, *Journal of Materials Chemistry A*, 2018, **6**, 3850–3856.
- 72 X. Guo, G. Fang, W. Zhang, J. Zhou, L. Shan, L. Wang, C. Wang, T. Lin, Y. Tang and S. Liang, Mechanistic Insights of  $\text{Zn}^{2+}$  Storage in Sodium Vanadates, *Advanced Energy Materials*, 2018, **8**, 1801819.
- 73 F. Wan, L. Zhang, X. Dai, X. Wang, Z. Niu and J. Chen, Aqueous rechargeable zinc/sodium vanadate batteries with enhanced performance from simultaneous insertion of dual carriers, *Nature Communications*, 2018, **9**, 1–11.

- 74 C. Xia, J. Guo, P. Li, X. Zhang and H. N. Alshareef, Highly Stable Aqueous Zinc-Ion Storage Using a Layered Calcium Vanadium Oxide Bronze Cathode, *Angewandte Chemie - International Edition*, 2018, **57**, 3943–3948.
- 75 B. Sambandam, V. Soundharrajan, S. Kim, M. H. Alfaruqi, J. Jo, S. Kim, V. Mathew, Y. K. Sun and J. Kim, K<sub>2</sub>V<sub>6</sub>O<sub>16</sub>·2.7H<sub>2</sub>O nanorod cathode: An advanced intercalation system for high energy aqueous rechargeable Zn-ion batteries, *Journal of Materials Chemistry A*, 2018, **6**, 15530–15539.
- 76 Z. Peng, Q. Wei, S. Tan, P. He, W. Luo, Q. An and L. Mai, Novel layered iron vanadate cathode for high-capacity aqueous rechargeable zinc batteries, *Chemical Communications*, 2018, **54**, 4041–4044.
- 77 B. Tang, J. Zhou, G. Fang, F. Liu, C. Zhu, C. Wang, A. Pan and S. Liang, Engineering the interplanar spacing of ammonium vanadates as a high-performance aqueous zinc-ion battery cathode, *Journal of Materials Chemistry A*, 2019, **7**, 940–945.
- 78 V. Soundharrajan, B. Sambandam, S. Kim, M. H. Alfaruqi, D. Y. Putro, J. Jo, S. Kim, V. Mathew, Y. K. Sun and J. Kim, Na<sub>2</sub>V<sub>6</sub>O<sub>16</sub>·3H<sub>2</sub>O Barnesite Nanorod: An Open Door to Display a Stable and High Energy for Aqueous Rechargeable Zn-Ion Batteries as Cathodes, *Nano Letters*, 2018, **18**, 2402–2410.
- 79 W. Li, K. Wang, S. Cheng and K. Jiang, A long-life aqueous Zn-ion battery based on Na<sub>3</sub>V<sub>2</sub>(PO<sub>4</sub>)<sub>2</sub>F<sub>3</sub> cathode, *Energy Storage Materials*, 2018, **15**, 14–21.
- 80 P. Hu, T. Zhu, X. Wang, X. Zhou, X. Wei, X. Yao, W. Luo, C. Shi, K. A. Owusu, L. Zhou and L. Mai, Aqueous Zn//Zn(CF<sub>3</sub>SO<sub>3</sub>)<sub>2</sub>//Na<sub>3</sub>V<sub>2</sub>(PO<sub>4</sub>)<sub>3</sub> batteries with simultaneous Zn<sup>2+</sup>/Na<sup>+</sup> intercalation/de-intercalation, *Nano Energy*, 2019, **58**, 492–498.
- 81 G. Li, Z. Yang, Y. Jiang, W. Zhang and Y. Huang, Hybrid aqueous battery based on Na<sub>3</sub>V<sub>2</sub>(PO<sub>4</sub>)<sub>3</sub>/C cathode and zinc anode for potential large-scale energy storage, *Journal of Power Sources*, 2016, **308**, 52–57.
- 82 F. Wang, E. Hu, W. Sun, T. Gao, X. Ji, X. Fan, F. Han, X. Q. Yang, K. Xu and C. Wang, A rechargeable aqueous Zn<sup>2+</sup>-battery with high power density and a long cycle-life, *Energy and Environmental Science*, 2018, **11**, 3168–3175.

- 83 P. He, M. Yan, G. Zhang, R. Sun, L. Chen, Q. An and L. Mai, Layered VS<sub>2</sub> Nanosheet-Based Aqueous Zn Ion Battery Cathode, *Advanced Energy Materials*, 2017, **7**, 1601920.
- 84 H. Qin, Z. Yang, L. Chen, X. Chen and L. Wang, A high-rate aqueous rechargeable zinc ion battery based on the VS<sub>4</sub>@rGO nanocomposite, *Journal of Materials Chemistry A*, 2018, **6**, 23757–23765.
- 85 T. Gupta, A. Kim, S. Phadke, S. Biswas, T. Luong, B. J. Hertzberg, M. Chamoun, K. Evans-Lutterodt and D. A. Steingart, Improving the cycle life of a high-rate, high-potential aqueous dual-ion battery using hyper-dendritic zinc and copper hexacyanoferrate, *Journal of Power Sources*, 2016, **305**, 22–29.
- 86 Z. Hou, X. Zhang, X. Li, Y. Zhu, J. Liang and Y. Qian, Surfactant widens the electrochemical window of an aqueous electrolyte for better rechargeable aqueous sodium/zinc battery, *Journal of Materials Chemistry A*, 2017, **5**, 730–738.
- 87 Z. Jia, B. Wang and Y. Wang, Copper hexacyanoferrate with a well-defined open framework as a positive electrode for aqueous zinc ion batteries, *Materials Chemistry and Physics*, 2015, **149**, 601–606.
- 88 R. Trócoli and F. la Mantia, An aqueous zinc-ion battery based on copper hexacyanoferrate, *ChemSusChem*, 2015, **8**, 481–485.
- 89 F. Grandjean, L. Samain and G. J. Long, Characterization and utilization of Prussian blue and its pigments, *Dalton Transactions*, 2016, **45**, 18018–18044.
- 90 B. Wang, Y. Han, X. Wang, N. Bahlawane, H. Pan, M. Yan and Y. Jiang, Prussian Blue Analogs for Rechargeable Batteries, , DOI:10.1016/j.isci.
- 91 G. Kasiri, R. Trócoli, A. Bani Hashemi and F. la Mantia, An electrochemical investigation of the aging of copper hexacyanoferrate during the operation in zinc-ion batteries, *Electrochimica Acta*, 2016, **222**, 74–83.
- 92 Y. Cheng, L. Luo, L. Zhong, J. Chen, B. Li, W. Wang, S. X. Mao, C. Wang, V. L. Sprenkle, G. Li and J. Liu, Highly Reversible Zinc-Ion Intercalation into Chevrel Phase Mo<sub>6</sub>S<sub>8</sub> Nanocubes and Applications for Advanced Zinc-Ion Batteries, *ACS Applied Materials and Interfaces*, 2016, **8**, 13673–13677.



- 93 W. Xu, C. Sun, K. Zhao, X. Cheng, S. Rawal, Y. Xu and Y. Wang, Defect engineering activating (Boosting) zinc storage capacity of MoS<sub>2</sub>, *Energy Storage Materials*, 2019, **16**, 527–534.
- 94 Z. Guo, Y. Ma, X. Dong, J. Huang, Y. Wang and Y. Xia, An Environmentally Friendly and Flexible Aqueous Zinc Battery Using an Organic Cathode, *Angewandte Chemie*, 2018, **130**, 11911–11915.
- 95 R. Cang, K. Ye, K. Zhu, J. Yan, J. Yin, K. Cheng, G. Wang and D. Cao, Organic 3D interconnected graphene aerogel as cathode materials for high-performance aqueous zinc ion battery, *Journal of Energy Chemistry*, 2020, **45**, 52–58.
- 96 Q. Zhao, W. Huang, Z. Luo, L. Liu, Y. Lu, Y. Li, L. Li, J. Hu, H. Ma and J. Chen, High-capacity aqueous zinc batteries using sustainable quinone electrodes, *Science Advances*, 2018, **4**, eaao1761.
- 97 C. Chen, Z. Gan, C. Xu, L. Lu, Y. Liu and Y. Gao, Electrosynthesis of poly(aniline-co-azure B) for aqueous rechargeable zinc-conducting polymer batteries, *Electrochimica Acta*, 2017, **252**, 226–234.
- 98 G. Dawut, Y. Lu, L. Miao and J. Chen, High-performance rechargeable aqueous Zn-ion batteries with a poly(benzoquinonyl sulfide) cathode, *Inorganic Chemistry Frontiers*, 2018, **5**, 1391–1396.
- 99 G. Wypych, in *Graphene*, Elsevier, 2019, pp. 9–84.
- 100 A. Krężel and W. Maret, The biological inorganic chemistry of zinc ions, *Archives of Biochemistry and Biophysics*, 2016, **611**, 3–19.
- 101 The 3G4G Blog: Smart Grids, <https://blog.3g4g.co.uk/search/label/Smart%20Grids>, (accessed April 4, 2020).